



HAL
open science

Numerical investigation of dislocation climb under stress and irradiation

Daphné da Fonseca, Fabien Onimus, Frédéric Momprou, Mihai Cosmin Marinica, Edouard de Sonis, Emmanuel Clouet, Thomas Jourdan

► To cite this version:

Daphné da Fonseca, Fabien Onimus, Frédéric Momprou, Mihai Cosmin Marinica, Edouard de Sonis, et al.. Numerical investigation of dislocation climb under stress and irradiation. *Acta Materialia*, 2022, 242, pp.118431. 10.1016/j.actamat.2022.118431 . cea-03884976

HAL Id: cea-03884976

<https://cea.hal.science/cea-03884976>

Submitted on 5 Dec 2022

HAL is a multi-disciplinary open access archive for the deposit and dissemination of scientific research documents, whether they are published or not. The documents may come from teaching and research institutions in France or abroad, or from public or private research centers.

L'archive ouverte pluridisciplinaire **HAL**, est destinée au dépôt et à la diffusion de documents scientifiques de niveau recherche, publiés ou non, émanant des établissements d'enseignement et de recherche français ou étrangers, des laboratoires publics ou privés.



Distributed under a Creative Commons Attribution 4.0 International License

Numerical investigation of dislocation climb under stress and irradiation

D. Da Fonseca^{a,d}, F. Onimus^b, F. Momprou^{c,d}, M.-C. Marinica^a, E. de Sonis^a,
E. Clouet^a, T. Jourdan^{a,*}

^a *Université Paris-Saclay, CEA, Service de Recherches de Métallurgie Physique, 91191, Gif-sur-Yvette, France*

^b *Université Paris-Saclay, CEA, Service de Recherches Métallurgiques Appliquées, 91191, Gif-sur-Yvette, France*

^c *Centre d'Elaboration de Matériaux et d'Etudes Structurales, CNRS UPR 8011, 29 rue J. Marvig, BP 94347, Toulouse cedex 4 31055, France*

^d *Université de Toulouse, UPS, F-31055 Toulouse, France*

Abstract

We investigate the influence of elastic properties of point defects on dislocation climb under stress and irradiation. For this purpose, elastic dipole tensors and diaelastic polarizabilities are evaluated in aluminum for vacancies and self-interstitial atoms in their stable and saddle configurations, using density functional theory calculations. These parameters are introduced in an object kinetic Monte-Carlo code and a continuous diffusion model to estimate the stress dependence of dislocation climb, using a dipole of straight dislocations. We show that both parameters have an influence on absorption of point defects under stress, in agreement with previous analytical models. However, the effect of dipole tensor is found only 5 times larger than polarizability, whereas models predict a factor up to 30. In addition, including polarizability reverses the stress angular dependence when a uniaxial stress is applied orthogonal to the dislocation line, so in general polarizability cannot be ignored for simulations under applied stress. Further comparison with analytical models shows that they give a good description of angular dependence, provided saddle point configuration of point defects is not too anisotropic. For vacancies, which are strongly anisotropic in their saddle configuration, models fail to reproduce quantitatively lattice effects on stress angular dependence observed in simulations. Calculations show that dislocation climb velocity under irradiation is expected to be the highest if the

stress is approximately orthogonal to the dislocation line, especially along the Burgers vector, and the lowest if the stress is applied close to the $\langle 100 \rangle$ direction with the largest projection on the dislocation line.

13 *Keywords:* Diffusion, Object kinetic Monte-Carlo, Irradiation creep,
14 Dislocation climb, SIPA

15 **1. Introduction**

16 Under irradiation and applied stress, metallic alloys exhibit a specific deformation process known as irradiation creep [1, 2]. The associated strain rate,
17 which may be much larger than the one associated to thermal creep, is related
18 to anisotropic microstructural changes. Among them, anisotropic formation
19 and growth of dislocation loops, resulting from the agglomeration of point defects (self-interstitial atoms, vacancies), have been observed [3, 4, 5, 6, 7, 8].
20 These processes have been explained by the reorientation of small clusters under stress [9] and/or the preferred absorption of self-interstitial atoms (SIAs)
21 and vacancies by some dislocation loops, depending on their orientation with
22 respect to the applied stress [10]. Other mechanisms have also been proposed.
23 They are based on climb-assisted glide of dislocations, whose anisotropic character may also come from the dependence of climb velocity on stress [11].
24

25 Two main models have been developed to explain the preferential climb of
26 some dislocation types under applied stress and irradiation. These two models
27 finely depend on the elastic properties of point defects, which couple to the
28 internal and applied strain fields and result in preferential absorption of point
29 defects at some dislocations. They both describe a point defect through its
30 elastic dipole, a tensor which describes how the point defect energy varies in a
31 strain field. The first model, known as stress induced preferred absorption due
32 to anisotropic diffusion (SIPA-AD)¹ [14, 15, 16, 17], relies on the anisotropy
33 of dipole tensors of point defects in their saddle configuration [18]. Due to
34
35
36

¹In some references it is called SIPA-SAPSE (stress induced preferred absorption due to saddle-point shape effect) [12, 13]. This name has the clear advantage to identify the physical

37 this anisotropy and to the lowering of crystal symmetry by an applied stress,
38 diffusion becomes anisotropic [19, 20]. This anisotropic diffusion is responsible
39 for different absorption “cross-sections” by dislocations and thus for preferred
40 absorption. The second model is the stress induced preferred absorption due
41 to inhomogeneity interaction (SIPA-I). It is also often simply called SIPA, as
42 it was developed first and remains very popular [21, 22, 23, 8]. It relies on the
43 dependence of dipole tensor on local stress, a phenomenon known as diaelastic
44 polarizability [24].

45 It is customary to quantify the effect of stress on absorption rate of defects
46 by dislocations by calculating absorption efficiencies, which are key quantities in
47 rate theory models. Previous analytical and numerical calculations have shown
48 that in iron and copper, absorption efficiencies under stress exhibit a higher de-
49 pendence on elastic dipole anisotropy than on polarizability, so that SIPA-AD
50 could be more than one order of magnitude larger than SIPA-I [14, 12, 16]. This
51 estimate relies on dipole tensors calculated by interatomic potentials, which can
52 differ substantially from dipole tensors evaluated by *ab initio* methods [25]. Sev-
53 eral approximations are made for the polarizability of the elastic dipole to make
54 analytical calculations tractable: the four-rank tensors characterizing this polar-
55 ization are assumed to be isotropic and identical for defects at stable and saddle
56 positions. In addition, it is unclear what consequences approximations made in
57 analytical models may have on the absorption rates of point defects [16]. For all
58 these reasons, it appears important to evaluate more precisely the amplitudes
59 of SIPA-AD and SIPA-I, *i.e.* the role of elastic dipole anisotropy and diaelastic
60 polarizabilities on absorption efficiencies of point defects by dislocations under
61 stress.

62 In the present work, we use two simulation methods to evaluate these ab-
63 sorption efficiencies in aluminum. The first one is an object kinetic Monte-Carlo

quantum responsible for the anisotropic behavior, since anisotropic diffusion (AD) can come from various physical quantities. However, SIPA-AD seems to be more widely used in the literature, so we keep this name here.

64 (OKMC) approach, which has already been used to determine absorption effi-
65 ciencies without applied stress [26]. The second one is a continuous diffusion
66 model (CDM) [27]. Both methods take into account point defect properties
67 at stable and saddle positions. To obtain a precise value of absorption effi-
68 ciencies, dipole and polarizability tensors are extracted from density functional
69 theory (DFT) calculations. Aluminum is chosen because it is nearly elastically
70 isotropic, so that isotropic elasticity can be used conveniently to predict absorp-
71 tion efficiencies [26].

72 This article is organized as follows. In section 2 diffusion of point defects
73 under stress is discussed and the existing models of absorption efficiency under
74 stress are shortly reviewed. Dipole tensors and diaelastic polarizabilities are cal-
75 culated in section 3. Absorption efficiencies of point defects by dislocations are
76 determined by OKMC and CDM and compared to existing models in section 4.

77 **2. Diffusion of point defects under stress and existing models of point** 78 **defect absorption efficiency**

79 *2.1. Diffusion under stress*

80 The migration of point defects to dislocations depends on their interaction
81 with the elastic field created by dislocations and the applied stress. A point de-
82 fect can be adequately described as an elastic dipole Π_{ij} [28, 29], which depends
83 on the local strain field if it is polarizable (summation over repeated indexes is
84 implied):

$$\Pi_{ij}(\boldsymbol{\varepsilon}) = P_{ij} + \alpha_{ijkl}\varepsilon_{kl}, \quad (1)$$

85 where $P_{ij} = \Pi_{ij}(0)$ is the elastic dipole without any effect of stress, α_{ijkl} the
86 diaelastic polarizability and ε_{ij} the local strain field at the position of the point
87 defect. The associated interaction energy can be expressed as [30]:

$$E = -P_{ij}\varepsilon_{ij} - \frac{1}{2}\varepsilon_{ij}\alpha_{ijkl}\varepsilon_{kl}. \quad (2)$$

88 Elastic dipoles and polarizabilities are in general different at stable and saddle
89 positions. In the following, superscript “s” means that a quantity is taken at
90 saddle position.

91 Dederichs and Schroeder have shown that the point defect flux can be written
 92 as a function of a renormalized diffusion tensor [20]

$$\tilde{D}_{ij}(\mathbf{r}) = \frac{1}{4}D_0 \sum_{\mathbf{h}} \hat{h}_i \hat{h}_j \exp\left(-\frac{E^{s,\mathbf{h}}(\mathbf{r})}{k_{\text{B}}T}\right), \quad (3)$$

93 where $E^{s,\mathbf{h}}(\mathbf{r})$ is the interaction energy as given by Eq. (2) for a point defect
 94 initially located at \mathbf{r} and performing a jump \mathbf{h} with associated unit vector $\hat{\mathbf{h}}$, D_0
 95 is the diffusion coefficient without stress, k_{B} the Boltzmann constant and T the
 96 temperature. The strain field in the interaction energy is taken at the location
 97 of the saddle point, which in the present case is $\mathbf{r} + \mathbf{h}/2$. The summation
 98 is performed on all nearest neighbors. The stress free diffusion coefficient is
 99 $D_0 = \kappa\nu_0 a^2 \exp(-E_0^{\text{m}}/k_{\text{B}}T)$, where $\kappa = 1$ for a vacancy and $\kappa = 2/3$ for a
 100 $\langle 100 \rangle$ -split dumbbell SIA. In this expression, a is the lattice parameter of the
 101 fcc matrix, ν_0 and E_0^{m} the attempt frequency and migration energy, respectively.

102 Using a Taylor expansion to second order in strain of the diffusion coefficient,
 103 Woo has clearly shown that different terms contribute to stress induced
 104 preferential absorption [16]. Even though in the present work this expansion is
 105 not used, it is useful to recall it to make the link with existing models. Let ε_{ij} be
 106 the sum of an applied strain $\varepsilon_{ij}^{\text{a}}$ and an internal strain $\varepsilon_{ij}^{\text{d}}$ due to a dislocation,
 107 which is assumed to weakly vary over distance a , so that $\varepsilon_{ij}^{\text{d}}(\mathbf{r} + \mathbf{h}/2) \approx \varepsilon_{ij}^{\text{d}}(\mathbf{r})$.

108 Inserting (2) into (3) leads to

$$\begin{aligned}
\tilde{D}_{ij}(\mathbf{r}) \approx & \underbrace{D_0 \delta_{ij}}_{1 - \text{stress free diffusion}} + \underbrace{\frac{1}{4} D_0 \frac{1}{k_B T} \sum_{\mathbf{h}} \hat{h}_i \hat{h}_j P_{kl}^{s, \mathbf{h}} \varepsilon_{kl}^d(\mathbf{r})}_{2 - \text{EID, first order}} \\
& + \underbrace{\frac{1}{4} D_0 \frac{1}{k_B T} \sum_{\mathbf{h}} \hat{h}_i \hat{h}_j P_{kl}^{s, \mathbf{h}} \varepsilon_{kl}^a}_{3 - \text{elastodiffusion, SIPA-AD (Woo)}} \\
& + \frac{1}{4} D_0 \frac{1}{k_B T} \sum_{\mathbf{h}} \hat{h}_i \hat{h}_j \left(\underbrace{\alpha_{klmn}^{s, \mathbf{h}}}_{4 - \text{SIPA-I}} + \underbrace{\frac{1}{k_B T} P_{kl}^{s, \mathbf{h}} P_{mn}^{s, \mathbf{h}}}_{5 - \text{SIPA-AD (Dederichs)}} \right) \varepsilon_{kl}^a \varepsilon_{mn}^d(\mathbf{r}) \\
& + \underbrace{\frac{1}{4} D_0 \frac{1}{k_B T} \sum_{\mathbf{h}} \hat{h}_i \hat{h}_j \left(\frac{1}{2} \alpha_{klmn}^{s, \mathbf{h}} + \frac{1}{2} \frac{1}{k_B T} P_{kl}^{s, \mathbf{h}} P_{mn}^{s, \mathbf{h}} \right) \varepsilon_{kl}^d(\mathbf{r}) \varepsilon_{mn}^d(\mathbf{r})}_{6 - \text{EID, second order}} \\
& + \underbrace{\frac{1}{4} D_0 \frac{1}{k_B T} \sum_{\mathbf{h}} \hat{h}_i \hat{h}_j \left(\frac{1}{2} \alpha_{klmn}^{s, \mathbf{h}} + \frac{1}{2} \frac{1}{k_B T} P_{kl}^{s, \mathbf{h}} P_{mn}^{s, \mathbf{h}} \right) \varepsilon_{kl}^a \varepsilon_{mn}^a}_{7 - \text{elastodiffusion, second order}}. \quad (4)
\end{aligned}$$

109 The first term corresponds to the diffusion tensor in the absence of stress. The
110 second term, which is related to the elastic interaction difference (EID) for
111 SIAs and vacancies, is responsible for the dislocation bias [31] to first order
112 (second order is the sixth term, it is always neglected). The third term is the
113 classical elastodiffusion term [20]. It has been identified by Woo as the main
114 contribution to SIPA [13, 16], called SIPA-AD. The fourth and fifth terms couple
115 the dislocation and applied strains and thus also lead to SIPA. The contribution
116 of polarizability corresponds to SIPA-I effect [21, 22, 23], whereas the product
117 of dipole tensors is the SIPA-AD effect as initially considered by Dederichs and
118 Schroeder [20]. In numerical simulations based on dipole tensor anisotropy, both
119 the third and fifth terms are included since the diffusion coefficient is kept in its
120 initial form (3) [15]. Finally, the sixth and seventh terms are second order terms
121 for EID and elastodiffusion. Although the latter can in principle contribute to
122 SIPA, it has been ignored in previous studies based on polarizabilities, which
123 all relied on analytical developments. Only the fourth term was considered.
124 However, here again, the second part of this term is present in numerical studies

125 using anisotropic dipole tensors.

126 *2.2. Models of point defect absorption efficiency under stress*

127 In the framework of rate theory, the effect of stress on point defect absorp-
 128 tion rate by dislocations is quantified by the so-called “absorption efficiencies”.
 129 These quantities relate the absorption rate of point defects to their average con-
 130 centration in the matrix. They are obtained by solving the diffusion problem
 131 around a sink, usually at stationary state [32, 33, 34, 35, 36]. Analytical ex-
 132 pressions of absorption efficiencies can be obtained only with simple geometries
 133 and simplified description of point defect properties. Taking into account the
 134 full complexity of Eq. (4) necessarily requires numerical simulations, as those
 135 performed in the present work.

136 Heald and Speight have given an expression for the absorption efficiency of
 137 defects by dislocations under a tensile stress of magnitude σ , if among terms 3
 138 to 7 in Eq. (4) only the fourth one is taken into account (SIPA-I) [23]. They
 139 assume that the polarizability tensor is the same at stable and saddle points
 140 and that it is isotropic, *i.e.*

$$\alpha_{ijkl} = \left(\alpha^K - \frac{2}{3} \alpha^\mu \right) \delta_{ij} \delta_{kl} + \alpha^\mu (\delta_{ik} \delta_{jl} + \delta_{il} \delta_{jk}), \quad (5)$$

141 where α^K and α^μ are the bulk and shear polarizabilities [37]. This approxima-
 142 tion amounts to considering the defect as an isotropic inhomogeneous Eshelby
 143 inclusion in the matrix. The dipole tensor is also assumed to be the same at
 144 stable and saddle points and is considered isotropic, *i.e.* $P_{ij} = P \delta_{ij}$. Woo has
 145 shown that the expression of Heald and Speight can be cast under the following
 146 form (HSW model) [38]:

$$Z^I(\boldsymbol{\sigma}) = Z^0 \left(1 + \frac{\Delta Z^I(\boldsymbol{\sigma})}{Z^0} \right), \quad (6)$$

147 with

$$\frac{\Delta Z^I(\boldsymbol{\sigma})}{Z^0} = \frac{Z^0}{2\pi} \frac{\delta L(\boldsymbol{\sigma})}{L^0} \quad (7)$$

$$Z^0 = \frac{2\pi}{\ln\left(\frac{4R}{|L^0|e^\gamma}\right)} \quad (8)$$

$$L^0 = \frac{Pb}{2\pi} \frac{1-2\nu}{1-\nu} \frac{1}{k_B T} \quad (9)$$

$$\frac{\delta L(\boldsymbol{\sigma})}{L^0} = \frac{\sigma}{\mu} \left[\frac{(1-2\nu)\alpha^K}{2(1+\nu)P} + \frac{\alpha^\mu}{3(1-2\nu)P} \left(-(1+\nu) + 3\nu(\mathbf{s} \cdot \mathbf{l})^2 + 3(\mathbf{s} \cdot \mathbf{b})^2 \right) \right] \quad (10)$$

148 (note that the 2π factor in Eq. (7) is missing in the expression of Woo). Z^0
 149 is the absorption efficiency without applied stress. In Eqs. (8)-(10), ν is the
 150 Poisson's ratio, μ is the shear modulus, \mathbf{b} is the Burgers vector ($b = |\mathbf{b}|$), \mathbf{l} is
 151 the dislocation line direction, γ is the Euler's constant ($\gamma \approx 0.577$) and R is
 152 the half-distance between dislocations, calculated as $R = (\pi\rho_d)^{-1/2}$ with ρ_d the
 153 dislocation density. The uniaxial stress is applied along \mathbf{s} , so that $\sigma_{ij} = \sigma s_i s_j$.
 154 Eqs. (6) to (10) are often given with different notations, considering the defect
 155 as an Eshelby inhomogenous inclusion. The link between the two formalisms is
 156 recalled in Appendix A. For the sake of completeness, we note that an expression
 157 with a similar dependence on stress orientation, in $(\mathbf{s} \cdot \mathbf{l})^2$ and $(\mathbf{s} \cdot \mathbf{b})^2$, was
 158 obtained by Wolfer and Ashkin [37].

159 With this model, the stress direction leading to the highest absorption ef-
 160 ficiency depends on the sign of α^μ/P (Eq. (10)). For an SIA in fcc metals,
 161 it is known that in its stable position, $\alpha^\mu > 0$ and $P > 0$ [39], so the model
 162 predicts that SIAs are more absorbed by a dislocation if the tensile stress is
 163 along the Burgers vector. For a vacancy, it is assumed in the literature that
 164 $\alpha^\mu > 0$ [23, 22], but $P < 0$, so the reverse behavior is expected.

165 Later, SIPA due to elastodiffusion (SIPA-AD) was investigated analytically
 166 by Skinner and Woo [13], Woo [16], and Borodin and Ryazanov [17]. The most
 167 general formula was derived by Borodin and Ryazanov. They showed that if
 168 only the three first terms in Eq. (4) are retained, and if the deviatoric part of
 169 the dipole tensor at saddle point is small, the absorption efficiency of a defect

170 can be written as

$$Z^{\text{AD}}(\boldsymbol{\sigma}) = Z^0 \left(1 + \frac{\Delta Z^{\text{AD},0}}{Z^0} + \frac{\Delta Z^{\text{AD,hydro}}(\boldsymbol{\sigma})}{Z^0} + \frac{\Delta Z^{\text{AD,dev}}(\boldsymbol{\sigma})}{Z^0} \right). \quad (11)$$

171 Contrary to the SIPA-I model described above, in this model, hereafter called
 172 B&R model, the defect has different properties at stable and saddle positions.
 173 The absorption efficiency Z^0 is still defined by Eqs. (8) and (9), but P is now re-
 174 lated to saddle point properties, *i.e.* $P = P^{\text{s}} = \text{Tr}(\mathbf{P}^{\text{s}})/3$. Z^0 thus corresponds
 175 to the absorption of an isotropic defect at saddle point. Saddle point anisotropy
 176 can have an influence on absorption efficiency even in the absence of applied
 177 stress [15, 40, 13, 17, 26, 41], this is taken into account through $\Delta Z^{\text{AD},0}$. The
 178 effect of stress on absorption efficiency can be decomposed into an hydrostatic
 179 term $\Delta Z^{\text{AD,hydro}}$ depending only on $\text{Tr}(\boldsymbol{\sigma})$, and a deviatoric term $\Delta Z^{\text{AD,dev}}$.
 180 Only the latter is of interest here, as we focus on the difference of absorption
 181 efficiencies for different orientations of applied stress. For a uniaxial stress, it
 182 reads [17, 42]

$$\frac{\Delta Z^{\text{AD,dev}}(\boldsymbol{\sigma})}{Z^0} = -\frac{\sigma}{4\mu} \frac{P^{\text{s}}}{k_{\text{B}}T} \left\{ d^{(2)} \left[(\mathbf{s} \cdot \mathbf{l})^2 - \frac{1}{3} \right] + d^{(3)} \sum_{p=1}^3 \left[(\mathbf{e}_p \cdot \mathbf{l})^2 (\mathbf{e}_p \cdot \mathbf{s})^2 - \frac{1}{9} \right] \right\}, \quad (12)$$

183 where \mathbf{e}_p ($p = 1, 2, 3$) are the unit vectors along the crystallographic axes.
 184 Factors $d^{(2)}$ and $d^{(3)}$ are related to the components of dipole tensors at saddle
 185 point. In an fcc structure, the dipole tensor of a defect jumping along [110] is
 186 of the form

$$\mathbf{P}^{\text{s}} = \begin{pmatrix} P_{11}^{\text{s}} & P_{12}^{\text{s}} & 0 \\ P_{12}^{\text{s}} & P_{11}^{\text{s}} & 0 \\ 0 & 0 & P_{33}^{\text{s}} \end{pmatrix}. \quad (13)$$

187 We then have $d^{(2)} = P_{12}^{\text{s}}/P^{\text{s}}$ and $d^{(3)} = (P_{11}^{\text{s}} - P_{33}^{\text{s}})/(2P^{\text{s}}) - P_{12}^{\text{s}}/P^{\text{s}}$.

188 It appears from Eq. (12) that the absorption efficiency does not depend
 189 on the orientation of uniaxial stress with respect to the Burgers vector, unlike
 190 SIPA-I. It is generally accepted that what is important for SIPA-AD is the
 191 orientation of stress with respect to the dislocation line direction \mathbf{l} , as shown in

192 the simplified model of Woo [16]:

$$\frac{\Delta Z^{\text{AD,dev}}(\boldsymbol{\sigma})}{Z^0} = \frac{3\sigma}{8\mu} \frac{P^s}{k_B T} \left(1 - \frac{P_1^s}{P^s}\right) \left[(\mathbf{s} \cdot \mathbf{l})^2 - \frac{1}{3}\right]. \quad (14)$$

193 This expression corresponds to Eq. (12) if $\mathbf{l} = \mathbf{e}_p$ for a given p , except that P_{11}^s
 194 in Eq. (12) is replaced by the eigenvalue P_1^s associated to the eigenvector along
 195 the jump direction (in practice P_{11}^s and P_1^s are very close, since $P_1^s = P_{11}^s + P_{12}^s$
 196 and $P_{12}^s \ll P_{11}^s$). For vacancies, $P^s < 0$ and $P_1^s/P^s > 1$ [43, 26], so a tensile
 197 stress applied along the dislocation line increases the absorption efficiency. For
 198 SIAs, $P^s > 0$ and $P_1^s/P^s > 1$, so the reverse behavior is expected. We note
 199 however that in the general case (Eq. (12)), it is clear that the orientation of
 200 stress with respect to crystallographic axes also plays a role.

201 Expressions for SIPA-AD and SIPA-I use only some terms in Eq. (4). In re-
 202 ality, all terms from 3 to 7 contribute to absorption efficiency modification under
 203 stress. As shown by Savino and Tomé [14], the third term, as a first-order term,
 204 should give the highest contribution. However, their results were obtained with
 205 crude estimates of polarizabilities and values of dipole tensors calculated by in-
 206 teratomic potentials. In addition, as shown in the previous paragraphs, various
 207 approximations underlie the analytical derivations. That is why, in the follow-
 208 ing, we evaluate the dipole tensors and polarizabilities for both stable and saddle
 209 configurations by DFT and introduce them into an OKMC code and a CDM
 210 model, which take into account the full complexity of diffusion under stress.
 211 We determine the relative importance of dipole anisotropy and polarizability by
 212 comparing these calculations to calculations without polarizability. The validity
 213 of expressions (7)-(10) and (12) is discussed, based on our simulation results.

214 **3. Point defect properties**

215 *3.1. Method*

216 Point defect properties can be calculated by atomistic simulations, from the
 217 energy difference between two simulation boxes containing a point defect, one

218 with applied homogeneous deformation ε and the other one without deforma-
 219 tion. Following Eq. (2), it reads, for a box of volume V [44, 29],

$$\Delta E(\varepsilon) = \frac{1}{2}\varepsilon_{ij}C_{ijkl}\varepsilon_{kl}V - P_{ij}\varepsilon_{ij} - \frac{1}{2}\varepsilon_{ij}\alpha_{ijkl}\varepsilon_{kl}. \quad (15)$$

220 The first term corresponds to the homogeneous deformation of the perfect crys-
 221 tal. It can be calculated separately with a dedicated simulation of a box without
 222 defect and subtracted from ΔE to retain only the contribution of the point de-
 223 fect. By fitting Eq. (15) without bulk contribution on calculations performed
 224 at different deformation levels, for different deformation types (shear, isotropic
 225 dilatation, etc.), it is possible to extract point defect dipole and polarizability
 226 tensors.

227 Another method consists in using the average residual stress on the simula-
 228 tion box [44, 29]:

$$\sigma_{ij}(\varepsilon) = \frac{1}{V} \frac{\partial \Delta E}{\partial \varepsilon_{ij}} = C_{ijkl}\varepsilon_{kl} - \frac{1}{V} (P_{ij} + \alpha_{ijkl}\varepsilon_{kl}). \quad (16)$$

229 Elastic dipoles are readily obtained from simulations with zero applied deforma-
 230 tion [45], after subtracting the spurious stress in the perfect simulation box [29].
 231 Polarizabilities can be extracted from a linear fit of the stress as a function of the
 232 deformation level, after subtraction of the contribution of the perfect crystal. If
 233 the dipole component is also deducted, the quantity $\Delta\sigma_{ij}(\varepsilon) = -\alpha_{ijkl}\varepsilon_{kl}/V$ is
 234 obtained.

235 To evaluate point defect properties in aluminum, DFT calculations are per-
 236 formed with VASP code [46, 47, 48, 49] using the projector augmented-wave
 237 (PAW) method [50, 51]. Calculations are performed including the s states
 238 $[\text{Ne}]3s^23p^1$. The exchange correlation energy is evaluated using the Perdew-
 239 Burke-Ernzerhof (PBE) generalized gradient approximation (GGA). The plane
 240 wave energy cutoff is set to 400 eV. Brillouin zone integration is performed
 241 with a Methfessel-Paxton broadening of 0.4 eV. Supercells with an SIA or a
 242 vacancy contain 256 ± 1 atoms. With such simulation cells, a dense shifted
 243 Monkhorst-Pack k -point mesh grid of $8 \times 8 \times 8$ points is necessary to obtain
 244 converged results, in agreement with previous results [52]. Each configuration

245 is relaxed using the conjugate gradient technique. The climbing image nudged
246 elastic band method (CI-NEB) [53] using 7 images is used in order to find saddle
247 points. A calculation is considered as converged when the forces on each atom
248 are lower than 0.002 eV/Å.

249 In the present study, dipole tensors are calculated with the stress method
250 (Eq. (16)). Simulations with interatomic potentials with different supercell sizes,
251 reported in supplementary material, show that the error on dipole tensor compo-
252 nents due to the interaction between the point defect and its periodic images [25]
253 is less than 1% (Fig. S1 and Table S1). Both energy and stress methods were
254 tested to determine polarizabilities. The convergence with the number of k -
255 points turned out to be faster with the stress method, in agreement with previ-
256 ous observations [54]. In addition, the stress method requires fewer deformation
257 types to extract polarizabilities, since the different stress components are related
258 to different combinations of α_{ijkl} coefficients. For these two reasons the stress
259 method is used. A list of the deformation types, with the corresponding values of
260 $-V\Delta\sigma_{ij}(\boldsymbol{\varepsilon}) = \alpha_{ijkl}\varepsilon_{kl}$, is given in Appendix B. Although the first deformation
261 is not necessary to determine coefficients for cubic and tetragonal symmetries, it
262 is calculated in order to check consistency of coefficients calculated by different
263 deformations. It also gives an estimate of the error on the coefficients, which
264 can roughly be estimated to a few eV. An additional source of error comes from
265 the interaction of the point defect with its periodic images [62]. Simulations
266 with interatomic potentials show that the error on polarizability tensor compo-
267 nents with supercells of 256 atoms is less than 10 %, except one component for
268 which it reaches 17 % (Fig. S2 and Table S1). Calculation of polarizabilities
269 at saddle points is computationally demanding, since a NEB calculation must
270 be performed for each deformation level of each deformation type. At least 5
271 deformation levels are used to perform the fit.

272 3.2. Results

273 Dipole and polarizability tensors are given in Table 1. Dipole tensor values
274 are slightly different from a previous DFT study [26], due to different DFT

275 settings and in particular denser k -point meshes used here. They are in good
 276 agreement with recent DFT calculations performed on the vacancy [55]. The
 277 relaxation volumes, deduced from the dipole tensor values through

$$\Delta V^r = \frac{\text{Tr } \mathbf{P}}{3K}, \quad (17)$$

278 where $K = (C_{11} + 2C_{12})/3$ is the bulk modulus, are also presented in Table 1.
 279 Altogether the values agree reasonably well with experiments, although the
 280 absolute value of the relaxation volume of the vacancy in its stable configuration
 281 is larger than the experimental value measured at 4 K. The tetragonal deviation
 282 from a cubic dipole tensor for the SIA in its stable configuration is in excellent
 283 agreement with the experimental value $P_{11} - P_{22} = 1.1 \pm 0.3$ eV [56].

284 As can be seen from Eq. (15), introducing polarizable point defects in a
 285 material leads to a variation of its elastic constants:

$$\Delta C_{ijkl} = -\frac{x}{\Omega} \alpha_{ijkl}, \quad (18)$$

286 where x is the atomic fraction of defects and Ω the atomic volume. This can be
 287 written under the more convenient form:

$$\frac{\Delta C_{ijkl}}{xC_{ijkl}} = -\frac{1}{\Omega C_{ijkl}} \alpha_{ijkl}. \quad (19)$$

288 Although α_{ijkl} has a tetragonal symmetry for SIAs, it is not possible to measure
 289 all components of the tensor experimentally. Assuming that SIA variants are
 290 equally distributed in the material, only data related to cubic symmetry can be
 291 extracted. Therefore it is possible to measure two shear polarizabilities

$$\alpha_{44}^* = \frac{1}{3} (\alpha_{44} + 2\alpha_{55}) \quad (20)$$

$$\alpha'^* = \frac{1}{3} \left(\frac{\alpha_{11} - \alpha_{12}}{2} + \frac{\alpha_{22} - \alpha_{12}}{2} + \frac{\alpha_{22} - \alpha_{23}}{2} \right) \quad (21)$$

292 and a bulk polarizability

$$\alpha^K = \frac{1}{3} \left(\frac{1}{3} (\alpha_{11} + 2\alpha_{12}) + \frac{2}{3} (\alpha_{22} + \alpha_{12} + \alpha_{23}) \right). \quad (22)$$

293 From Eq. (19) it is then possible to compute the influence of defects on C_{44} ,
 294 $C' = (C_{11} - C_{12})/2$ and K . DFT results in Tab. 1 show that SIAs contribute

295 much more to the change of elastic constants than vacancies, in agreement
296 with experimental results [57]. Vacancies make the material more compliant
297 in compression and in shear, while SIAs are compliant in shear and stiff in
298 compression. These variations are consistent with trends inferred from simple
299 arguments in early works on SIPA-I [23]. The fact that SIAs are compliant in
300 shear, which is not so intuitive, was proved with analytical models and atomistic
301 calculations [58]. Experimental measurements also support this result. The
302 variation in the two shear moduli, C_{44} and C' , was measured in aluminum after
303 electron irradiation at low temperature, where only Frenkel pairs are created
304 (Tab. 1). Negative values were obtained, in agreement with present results.
305 We note also that $|\Delta C_{44}/xC_{44}| > |\Delta C'/xC'|$, which has been shown to be
306 typical of fcc metals containing 100-dumbbells [58, 57]. Finally and perhaps
307 most importantly, the magnitude of the change of shear moduli due to both
308 vacancies and SIAs agrees well with experimental results. The change in bulk
309 modulus upon introduction of point defects has not been measured in aluminum
310 but it is expected to be small, following results obtained in Cu [59, 60]. This is
311 confirmed by our calculations.

312 We end this section with a comment on the calculation of polarizabilities
313 with interatomic potentials. Early calculations were made with simple pair
314 potentials for stable [58] and saddle [30, 61] configurations. The obtained polar-
315 izabilities were found consistent with the variation of elastic constants measured
316 experimentally [58, 30]. However, later simulations in Cu with more physical
317 potentials were shown to produce results at variance with experiments [62], with
318 values of opposite signs. We encountered similar problems with potentials in
319 aluminum, which highlights the need for DFT calculations to evaluate polariz-
320 abilities.

Table 1: Dipole and polarizability tensors of vacancies and SIAs in their stable and saddle configurations. Entries which are not filled are zero by symmetry. Relaxation volumes and change of elastic constants due to defects, deduced from dipole tensors and polarizabilities, respectively, are compared to experimental values. Elastic constants determined by DFT are $C_{11} = 111.4$ GPa, $C_{12} = 60.7$ GPa and $C_{44} = 33.1$ GPa.

	vacancy (stable)	vacancy (saddle) ([100] \rightarrow [010])	SIA (stable) ([100])	SIA (saddle) ([100] \rightarrow [010])
P_{11} (eV)	-2.49	-2.15	18.71	18.57
P_{22} (eV)	$= P_{11}$	$= P_{11}$	17.80	$= P_{11}$
P_{33} (eV)	$= P_{11}$	1.96	$= P_{22}$	18.40
P_{12} (eV)		-0.22		1.45
α_{11} (eV)	23	41	-10	4
α_{33} (eV)	$= \alpha_{11}$	-3	-13	-8
α_{44} (eV)	4	7	103	73
α_{55} (eV)	$= \alpha_{44}$	$= \alpha_{44}$	41	$= \alpha_{44}$
α_{66} (eV)	$= \alpha_{44}$	15	$= \alpha_{55}$	62
α_{36} (eV)		9		0
α_{16} (eV)		-1		-12
α_{45} (eV)		10		25
α_{23} (eV)	$= \alpha_{12}$	$= \alpha_{13}$	-45	$= \alpha_{13}$
α_{13} (eV)	$= \alpha_{12}$	2	$= \alpha_{12}$	-56
α_{12} (eV)	13	19	-60	-71
$\Delta V^r/\Omega$ (sim.)	-0.31	-0.10	2.27	
$\Delta V^r/\Omega$ (exp.)	$-0.05 \pm 0.05^{(a)}$ $-0.36^{(b)}$	$-0.19^{(d)}$	$1.9 \pm 0.2^{(a,c)}$	
$\frac{\Delta C_{44}}{xC_{44}}$ (sim.)	-1.2		-18.1	
$\frac{\Delta C_{44}}{xC_{44}}$ (exp.) ^(e)			-23 ± 2	
$\frac{\Delta C'}{\Delta C'}$ (sim.)	-1.9		-8.2	
$\frac{\Delta C'}{\Delta C'}$ (exp.) ^(e)			-13 ± 2	
$\frac{\Delta K}{xK}$ (sim.)	-2		5	

^(a) Measurement at 4 K, Reference [63].

^(b) Measurement at 700 K, Reference [64].

^(c) Reference [65].

^(d) Reference [66], using formation volume of Ref. [64].

^(e) After subtraction of the anharmonic effect due to volume expansion [57]. This value corresponds to the sum of SIA and vacancy contributions, but it is often considered that vacancy contribution is small [39, 57], which is confirmed by measurements on quenched samples [67].

321 **4. Effect of stress orientation on point defect absorption by disloca-**
322 **tions**

323 *4.1. Methods*

324 In this part, we evaluate the absorption efficiencies of point defects by dis-
325 locations in the configuration shown in Fig. 1. The system contains two dis-
326 locations of opposite Burgers vectors $\mathbf{b} = \pm a/2[10\bar{1}]$ and line direction $\mathbf{l} =$
327 $1/\sqrt{6}[\bar{1}2\bar{1}]$. The vector normal to the glide plane is $\mathbf{n} = 1/\sqrt{3}[111]$. The lattice
328 is rotated to align the dislocations along the direction \mathbf{u}_z of the orthorhombic
329 box and the Burgers vectors along \mathbf{u}_x . The dimension of the system is d along
330 y and $2d$ along x , with $d = 100$ nm, and the dislocations are located at $d/2$ and
331 $3d/2$ along x . This corresponds to a dislocation density $\rho_d = 10^{14}$ m⁻², which
332 is typical of steady state dislocation densities of irradiated microstructures [68].
333 Along z , the system consists of a thin slab of 1 nm. Periodic boundary condi-
334 tions are used in the three directions. This arrangement of dislocations was used
335 in a previous study [26], it ensures a proper convergence of the strain field when
336 the contribution of dislocations in periodic replica is taken into account [69], if
337 the strain field is evaluated with isotropic elasticity. It has been checked pre-
338 viously that in aluminum, using isotropic elasticity has a negligible effect on
339 absorption efficiencies [26], so we use this approximation here. This also per-
340 mits to increase the computational efficiency of OKMC simulations. The shear
341 modulus is $\mu = 26$ GPa and the Poisson's ratio is $\nu = 0.35$ [26]. Other disloca-
342 tion arrangements could have been chosen; with such dislocation densities they
343 would give slightly different values of absorption efficiencies [35]. However, the
344 dependence of absorption efficiencies on stress orientation is expected to be the
345 same.

346 To determine absorption efficiencies, vacancies and SIAs are considered sep-
347 arately. Point defects are uniformly generated in the system and they are ab-
348 sorbed if they reach one of the cylinders of radius $r_c = 2b$ centered on disloca-
349 tions. The mean field equation describing the evolution of point defect average

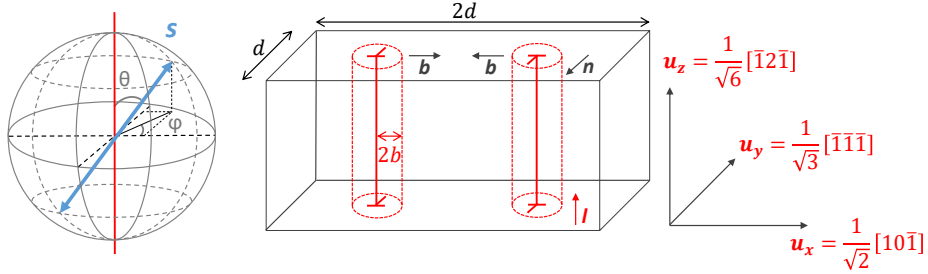


Figure 1: System simulated containing a dipole of straight dislocations. A tensile stress σ is applied along \mathbf{s} , given by the two angles (θ, φ) .

350 concentration \bar{C} is

$$\frac{d\bar{C}}{dt} = G - Z\rho_d D_0 \bar{C}, \quad (23)$$

351 where G is the creation rate. The absorption efficiency is deduced at steady
352 state from the measurement of \bar{C} :

$$Z = \frac{G}{\rho_d D_0 \bar{C}}. \quad (24)$$

353 A convenient method to determine \bar{C} is object kinetic Monte-Carlo [26].
354 Point defects are introduced at a constant rate in the simulation box. They
355 perform atomic jumps until they are absorbed by one of the dislocations. For
356 a point defect located at \mathbf{r} , jump frequencies are calculated for each jump \mathbf{h} ,
357 using the following expression:

$$\Gamma^{\mathbf{h}}(\mathbf{r}) = \nu_0 \exp\left(-\frac{E_0^{\text{m}} + E^{\text{s}}(\mathbf{r} + \mathbf{h}/2) - E^{\text{e}}(\mathbf{r})}{k_{\text{B}}T}\right), \quad (25)$$

358 where, as in section 2, ν_0 and E_0^{m} are the attempt frequency and the migra-
359 tion energy without elastic interactions, E^{e} and E^{s} are the interaction energies
360 with the local strain field at stable and saddle points, respectively (Eq. (2)).
361 Events (defect jumps and creation of point defects) are chosen following the
362 residence time algorithm [70, 71]. Transition of SIAs to $\langle 110 \rangle$ crowdion config-
363 uration, highlighted recently in copper under high local shear strain [72], is not
364 considered. More details on OKMC simulations can be found in Ref. [26].

365 For a given creation rate, it is possible to determine Z by calculating the
366 average number of point defects in the simulation box at steady state (Eq. (24)).

367 The physical time of the simulations is chosen to ensure the convergence of Z . To
 368 provide a confidence interval, the standard deviation is computed with a block-
 369 averaging procedure [73]. On all graphs, the error bars in figures correspond to
 370 the standard deviation.

371 An alternative to OKMC is the continuous diffusion model (CDM), as de-
 372 scribed in Ref. [27]. This approach has been shown to produce results in close
 373 agreement with reference OKMC simulations; in particular, it can properly
 374 handle the interaction of point defects with sinks in their stable and saddle po-
 375 sitions, as explicitly done in OKMC. The equation to be solved is based on the
 376 expression of the renormalized diffusion tensor given in Eq. (3):

$$G - \nabla \cdot \mathbf{J} = 0, \quad (26)$$

377 with

$$\mathbf{J}(\mathbf{r}) = -\tilde{\mathbf{D}}(\mathbf{r})\nabla u(\mathbf{r}). \quad (27)$$

378 In this equation, u is a renormalized concentration, which accounts for the
 379 concentrations of the different configurations of defects in their stable position
 380 (for SIAs) [20, 27]. Contrary to OKMC, CDM is a local approach, *i.e.* it
 381 amounts to taking E^s in Eq. (25) at \mathbf{r} instead of $\mathbf{r} + \mathbf{h}/2$. In practice, for
 382 weakly varying elastic fields, this approximation is valid. CDM calculations are
 383 similar to phase field calculations in this context [41].

384 Since it is deterministic in nature, CDM produces results which are free
 385 of statistical error. However, the finite element solving of the continuity equa-
 386 tion (26) may be quite CPU and memory demanding for large three-dimensional
 387 systems, as fine meshing is required near the sink where concentrations and elas-
 388 tic fields vary steeply. Therefore, this method is especially useful for systems
 389 which are invariant along at least one direction. This is the case of the con-
 390 figuration shown in Fig. 1, which is invariant along z . Although absorption
 391 efficiencies can be obtained with a two-dimensional system, we use a thin slab
 392 of 1 nm along z and impose periodic boundary conditions, as in OKMC.

393 In the following, simulations are performed at $T = 300$ K. A uniaxial tensile
 394 stress of 100 MPa is applied along (θ, φ) (Fig. 1). Although this value is rather

395 high for aluminum (the yield stress of very large grained pure aluminum is
 396 around 10 MPa), it permits to obtain a better convergence with OKMC. We
 397 have checked, by varying the stress amplitude, that at such levels of stress the
 398 absorption efficiency is linear in σ . So the results can easily be extrapolated to
 399 lower values of stress. The effect of elastodiffusion is investigated with OKMC,
 400 which is our reference method. We check that in this case, CDM produces
 401 results in agreement with OKMC. To determine the effect of polarizability, we
 402 subtract the absorption efficiencies obtained with and without polarizability.
 403 As we need very high accuracy on the absorption efficiencies to perform the
 404 subtraction, CDM is used in this case.

405 *4.2. Results*

406 *4.2.1. SIPA-AD*

407 As explained above, for SIPA-AD the interaction energy of point defects is
 408 based solely on elastic dipoles. To evaluate this first mechanism, we start with
 409 OKMC simulations. A 3D map representing the influence of tensile stress ori-
 410 entation on absorption efficiency is shown in Fig. 2. We represent the difference
 411 of absorption efficiencies for a uniaxial stress of magnitude σ and a hydrostatic
 412 stress with the same value of $\text{Tr}(\boldsymbol{\sigma})$, called $\Delta Z_{\text{I}}^{\text{AD}}$ for SIAs and $\Delta Z_{\text{V}}^{\text{AD}}$ for va-
 413 cancies. This quantity corresponds to $\Delta Z^{\text{AD,dev}}$ in the decomposition shown in
 414 Eq. (11). From Fig. 2 we see that vacancy absorption is increased if the stress
 415 is applied close to a direction ($\theta = 30^\circ, \varphi = 90^\circ$). Directions that favor SIA
 416 absorption are more or less spread on a strip tilted with respect to the plane
 417 orthogonal to the line direction.

418 To provide a more quantitative representation and facilitate the comparison
 419 with CDM and B&R model (Eq. (12)), ΔZ^{AD} is plotted in Figs. 3 and 4 as a
 420 function of θ , for $\varphi = 0^\circ$ (in the slip plane (\mathbf{l}, \mathbf{b})) and $\varphi = 90^\circ$ (in the climb
 421 plane (\mathbf{l}, \mathbf{n})). Results obtained with CDM are in very good agreement with
 422 OKMC, which validates CDM to calculate sink strengths in this configuration.
 423 B&R model is able to qualitatively reproduce the effect of stress on absorption
 424 efficiency. In particular, the dependence on φ is correctly taken into account,

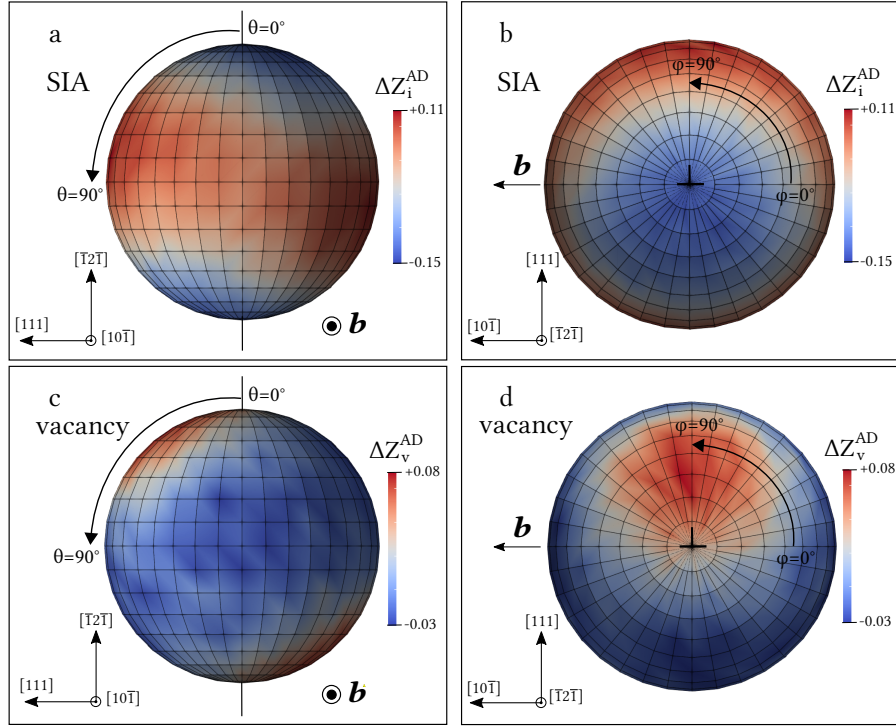


Figure 2: Difference of absorption efficiency ΔZ^{AD} (see text for the definition) of a straight dislocation dipole in relation to the tensile stress orientation, represented on a unit sphere by a color scale for SIA-AD mechanism when only P_{ij} is accounted for in the interaction energy. A tensile stress of 100 MPa is applied, scanning space with a 10° step. The dislocation is along $[\bar{1}\bar{2}\bar{1}]$ and the Burgers vector is along $\pm[10\bar{1}]$. The SIA results are presented in (a) and (b) and the vacancy results in (c) and (d). For the sake of clarity only one dislocation is schematically represented.

425 unlike the model of Woo which only depends on θ (not shown). However,
 426 the amplitude of ΔZ^{AD} is underestimated with B&R model, especially for the
 427 vacancy with a factor up to 3 at $\theta = 30^\circ$ and $\varphi = 90^\circ$, where the absorption
 428 efficiency is maximum.

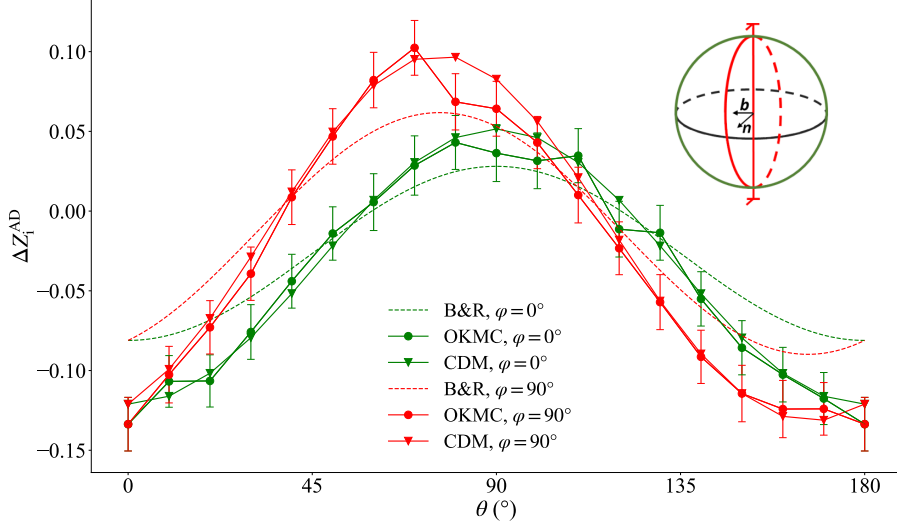


Figure 3: Difference of absorption efficiency ΔZ^{AD} (see text for the definition) of a straight dislocation dipole for SIAs as a function of θ (angle between tensile stress and dislocation line \mathbf{l}) for SIPA-AD mechanism, with only P_{ij} accounted for in the interaction energy. Results obtained by OKMC and CDM are compared. The analytical B&R model of Eq. (12) is shown in dashed lines. The absorption efficiency is presented for two values of φ : $\varphi = 0^\circ$, *i.e.* in a plane containing \mathbf{l} and \mathbf{b} and $\varphi = 90^\circ$, *i.e.* in a plane containing \mathbf{l} and \mathbf{n} .

4.2.2. SIPA-I

430 To determine the effect of polarizability, absorption efficiencies obtained with
 431 dipole tensors only are subtracted from those obtained with both dipole and
 432 polarizability tensors taken into account. These quantities are noted ΔZ^{I} . As
 433 discussed above, CDM is used for the two calculations to obtain results free
 434 from statistical errors.

435 Absorption efficiencies of SIAs and vacancies are the highest along two dif-
 436 ferent specific directions of applied stress (Fig. 5). Absorption of SIAs is more

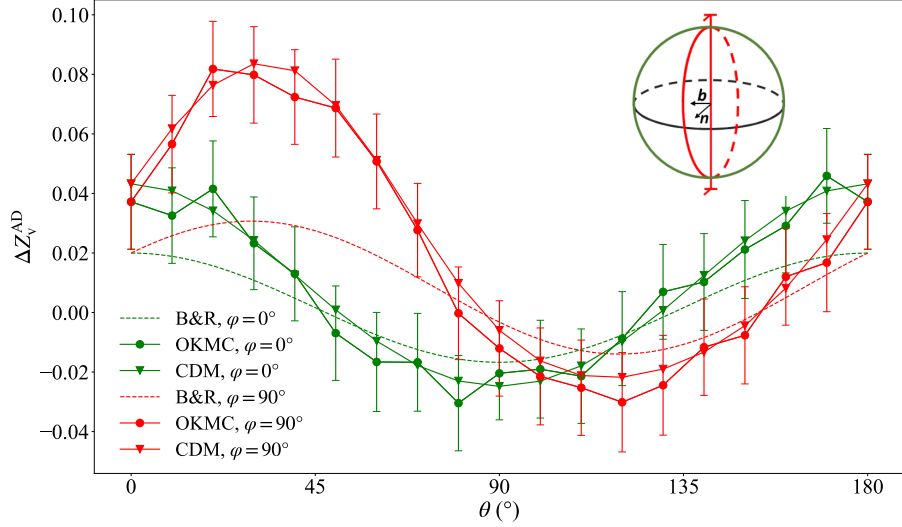


Figure 4: Difference of absorption efficiency ΔZ_v^{AD} (see text for the definition) of a straight dislocation dipole for vacancies as a function of θ (angle between tensile stress and dislocation line l) for SIPA-AD mechanism, with only P_{ij} accounted for in the interaction energy. Results obtained by OKMC and CDM are compared. The analytical B&R model of Eq. (12) is shown in dashed lines. The absorption efficiency is presented for two values of φ : $\varphi = 0^\circ$, *i.e.* in a plane containing l and b and $\varphi = 90^\circ$, *i.e.* in a plane containing l and n .

437 efficient if the stress is applied along the Burgers vector, in agreement with
 438 early estimates of SIPA-I [21, 23, 38]. The influence of polarizability on va-
 439 cancy absorption under stress is more surprising. It appears quite similar to
 440 the effect of dipole tensor anisotropy, with a direction of preferential absorption
 441 along ($\theta = 30^\circ$, $\varphi = 90^\circ$). With the existing SIPA-I model, one expects a low
 442 absorption rate if the stress is applied along the Burgers vector and a higher
 443 absorption rate for other stress orientations.

444 To provide a more quantitative comparison with HSW model (Eqs. (7)-(10)),
 445 which assumes that point defects have the same isotropic properties at stable
 446 and saddle positions, the values of dipole tensor P and polarizabilities α^μ and
 447 α^K are deduced from properties of defects in Tab. 1 taken at stable position. P ,
 448 calculated as $\text{Tr}(\mathbf{P})/3$, is equal to 18.10 eV for SIAs and -2.49 eV for vacancies.

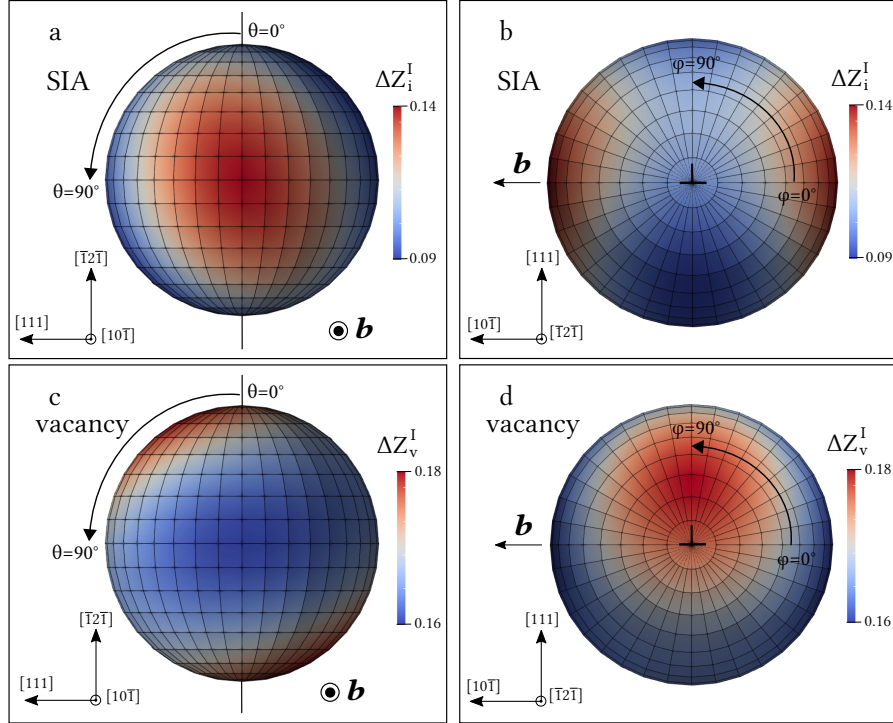


Figure 5: Absorption efficiency increment ΔZ^I of point defects by a straight dislocation dipole in relation to the tensile stress orientation, represented on a unit sphere by a color scale, due to polarizability α_{ijkl} (SIPA-I). Values are obtained by CDM. They result from the difference between absorption efficiencies with P_{ij} and α_{ijkl} considered and with only P_{ij} included. A tensile stress of 100 MPa is applied, scanning space with a 10° step. The dislocation is along $[\bar{1}2\bar{1}]$ and the Burgers vector is along $\pm[10\bar{1}]$. The SIA results are presented in (a) and (b) and the vacancy results in (c) and (d).

449 Shear polarizability can be expressed as a Voigt average

$$\alpha^\mu = \frac{3}{5}\alpha_{44}^* + \frac{2}{5}\alpha'^*, \quad (28)$$

450 where α_{44}^* and α'^* are given by Eqs. (20) and (21) respectively. We have
 451 $\alpha^\mu = 45.6$ eV for SIAs and $\alpha^\mu = 4.4$ eV for vacancies. Bulk polarizability,
 452 as calculated with Eq. (22), is $\alpha^K = -40.7$ eV for SIAs and $\alpha^K = 16.3$ eV for
 453 vacancies.

454 The effect of SIPA-I is usually discussed for a tensile stress orthogonal to the
 455 dislocation line ($\theta = 90^\circ$), either along the Burgers vector ($\varphi = 0^\circ$) or orthogonal
 456 to it ($\varphi = 90^\circ$) [23]. The variation of absorption efficiency with φ , with $\theta = 90^\circ$,
 457 is shown in Figs. 6 and 7 for SIAs and vacancies, respectively. Some terms are
 458 dropped in Eq. (6), which may explain why results are shifted with respect to
 459 CDM. This shift is not relevant to our purpose. Leaving this aspect aside, the
 460 agreement between CDM results and HSW model for $\theta = 90^\circ$ is remarkable
 461 for the two defects. Results for $\theta = 30^\circ$, including the direction where ΔZ_v^I is
 462 maximum, are also reported in these figures. The analytical solution departs
 463 appreciably from CDM, especially for the vacancy. The amplitude of SIPA-I for
 464 the vacancy is lower than the result from CDM by more than a factor two.

465 4.3. Discussion

466 4.3.1. SIPA-AD

467 The contribution of intrinsic dipole anisotropy at saddle configuration to
 468 SIPA (SIPA-AD) has been discussed by several authors [19, 20, 15, 13, 16, 17].
 469 It was shown that the absorption efficiency is mostly dependent on the direction
 470 of uniaxial stress with respect to the dislocation line [15, 13]. Under stress,
 471 the diffusion tensor becomes anisotropic, owing to saddle point anisotropy. A
 472 dislocation orthogonal to the direction of fastest diffusion will capture more
 473 point defects than a dislocation collinear to it, because its “cross section” for
 474 defect absorption is higher (the term “cross-section” is only strictly valid for
 475 purely 1D diffusion, *i.e.* for an infinitely large effect of stress). Directions of
 476 fast diffusion depend on the values of dipole tensor at saddle configuration.

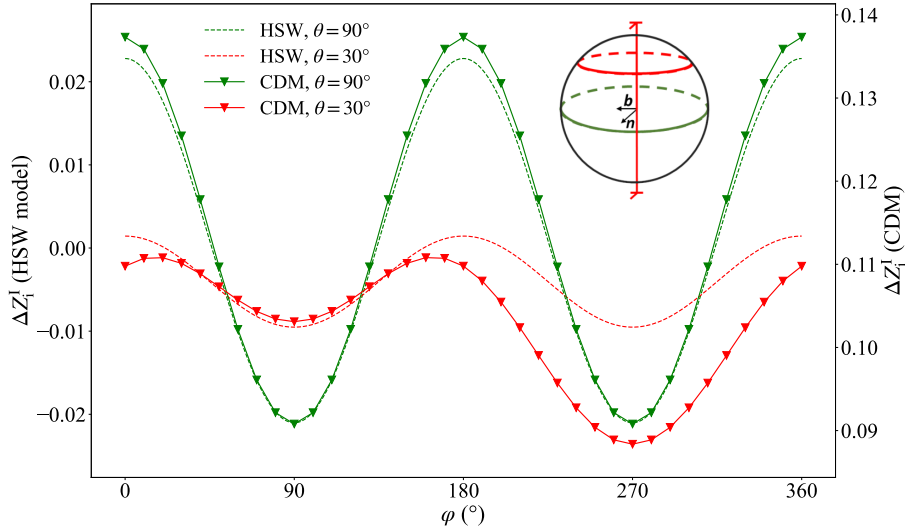


Figure 6: Increment of absorption efficiency ΔZ_i^I due to polarizability of SIAs, as a function of φ , for two values of θ (30° and 90°). Results are obtained with CDM and compared to HSW model given by Eqs. (7)-(10).

477 Vacancies diffuse preferentially in a plane orthogonal to the applied stress [74],
 478 which explains why vacancy absorption is enhanced when the tensile direction
 479 is collinear to the dislocation line. The behavior of SIAs is explained with the
 480 same reasoning [16].

481 We have seen in Fig. 2 that our simulations and B&R model are in quali-
 482 tative agreement with these conclusions. However, the direction of maximum
 483 absorption of vacancies is shifted by about 30° with respect to the line direc-
 484 tion in the plane defined by (\mathbf{l}, \mathbf{n}) ($\varphi = 90^\circ$). Likewise, the strip of maximum
 485 absorption for SIAs is tilted, with a maximum at around $\theta = 70^\circ$ in the plane
 486 (\mathbf{l}, \mathbf{n}) and $\theta = 90^\circ$ in the plane (\mathbf{l}, \mathbf{b}) ($\varphi = 0^\circ$). These discrepancies can be ex-
 487 plained by lattice effects, which are not all taken into account in Woo's approach
 488 (Eq. (14)), unlike B&R model (Eq. (12)).

489 To explain these results, we consider a uniaxial stress $\sigma_{ij} = \sigma s_i s_j$, with
 490 $s_1 = \sin \alpha \cos \beta$, $s_2 = \sin \alpha \sin \beta$, $s_3 = \cos \beta$ the three direction cosines of \mathbf{s} in

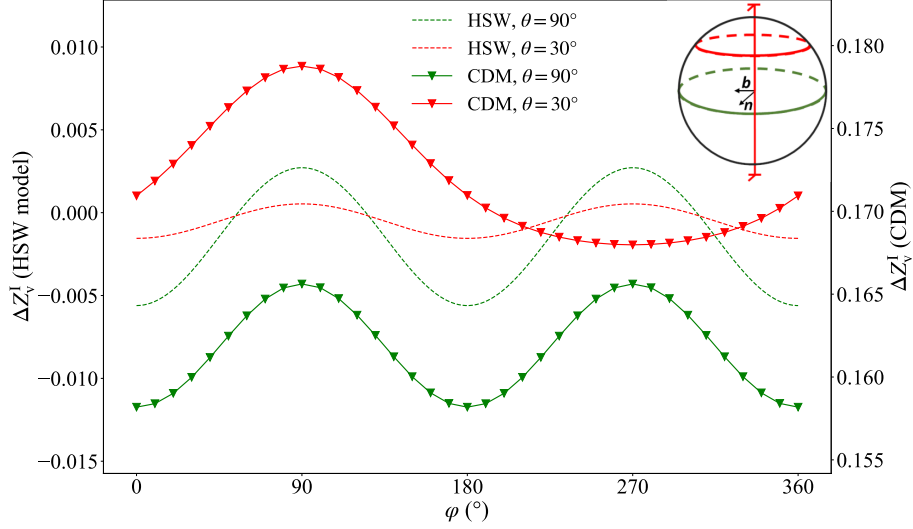


Figure 7: Increment of absorption efficiency ΔZ_v^I due to polarizability of vacancies, as a function of φ , for two values of θ (30° and 90°). Results are obtained with CDM and compared to HSW model given by Eqs. (7)-(10).

491 the basis $([100], [010], [001])$. We have

$$\varepsilon_{ij} = \frac{\sigma}{E} (s_i s_j (1 + \nu) - \nu \delta_{ij}), \quad (29)$$

492 with $E = 2\mu(1 + \nu)$ Young's modulus. We consider a jump along $[110]$, for
 493 which the dipole tensor at saddle position is given by Eq. (13). Neglecting the
 494 polarizability, the saddle point energy reads

$$E^s = -\frac{\sigma}{E} (P_{11}(1 + \nu) \sin^2 \alpha - 2\nu P_{11} + P_{33}(1 + \nu) \cos^2 \alpha - \nu P_{33} \\ + P_{12}(1 + \nu) \sin^2 \alpha \sin 2\beta). \quad (30)$$

495 Given the signs of the dipole tensor components of a vacancy (see Tab. 1),
 496 it is clear that the energy is minimum for $\alpha = 0^\circ$, *i.e.* for a stress applied along
 497 $[001]$. For the SIA, since $P_{12} > 0$, we must have $\beta = 45^\circ$. In addition, with
 498 $P_{11} + P_{12} > P_{33}$ the energy is minimum for $\alpha = 90^\circ$. This means the stress
 499 must be applied along the jump direction to minimize the saddle point energy.

500 As already discussed, to obtain the maximum absorption efficiency by a
 501 dislocation, one must favor the jumps which are as orthogonal as possible to

502 this dislocation. For a dislocation along $\mathbf{l} = [\bar{1}2\bar{1}]/\sqrt{6}$, there are two jumps
 503 which are orthogonal to the dislocation line, highlighted in red in Fig. 8-(a).
 504 These jumps are favored if the stress is applied along $[010]$. This configuration
 505 corresponds to $\theta = 35^\circ$, in close agreement with our OKMC and CDM results
 506 ($\theta \approx 33^\circ$) and B&R results ($\theta = 29^\circ$). The absorption rate of SIAs should be
 507 large if the stress is applied along the direction of the two jumps orthogonal to
 508 the line direction, represented in green in Fig. 8-(b). The jump direction is along
 509 \mathbf{b} , and it can be seen in Fig. 2 that indeed, this direction is located in the strip
 510 of high absorption rates. It is actually the direction of highest absorption rate
 511 in the plane (\mathbf{l}, \mathbf{b}) ($\varphi = 0^\circ$). From Fig. 2 it appears that maximum absorption
 512 rates are obtained in a plane (\mathbf{l}, \mathbf{n}) ($\varphi = 90^\circ$). For a stress applied in this plane,
 513 the projection of \mathbf{s} on the jumps represented in red in Fig. 8-(b) is the highest
 514 for $\theta = 71^\circ$; these four jumps are not orthogonal to the dislocation, but their
 515 projection on \mathbf{l} is small. The fact that four jumps contribute to SIA diffusion
 516 enhancement in this case explains why the absorption rate is even higher than
 517 for \mathbf{s} along \mathbf{b} . The value of θ found is very close to OKMC and CDM results
 518 ($\theta = 76^\circ$, Fig. 3) and B&R results ($\theta = 76^\circ$). The variation of θ from 90°
 519 to 71° as φ varies from 0° to 90° explains the tilted strip in Fig. 2. Finally,
 520 we note that in this discussion, the strain field of the dislocation has not been
 521 considered. This validates the assumption of Woo to neglect the dislocation
 522 field in the analytical treatment [16]. Fully considering lattice effects as in B&R
 523 model appears necessary to obtain a good agreement with OKMC and CDM. We
 524 note that although second order terms in Eq. (4) (fifth term and second part of
 525 seventh term) can in principle also contribute to SIPA-AD, they certainly have
 526 a very small impact as they are included in OKMC and CDM but not in B&R
 527 model.

528 Even though B&R model successfully reproduces lattice effects, the magni-
 529 tude of ΔZ^{AD} is significantly different from our calculations for both defects.
 530 This is especially the case for the vacancy. In the direction of applied stress
 531 where the absorption efficiency is the highest, the discrepancy reaches a fac-
 532 tor of around 3. For this direction, the effects of anisotropy of dipole tensor

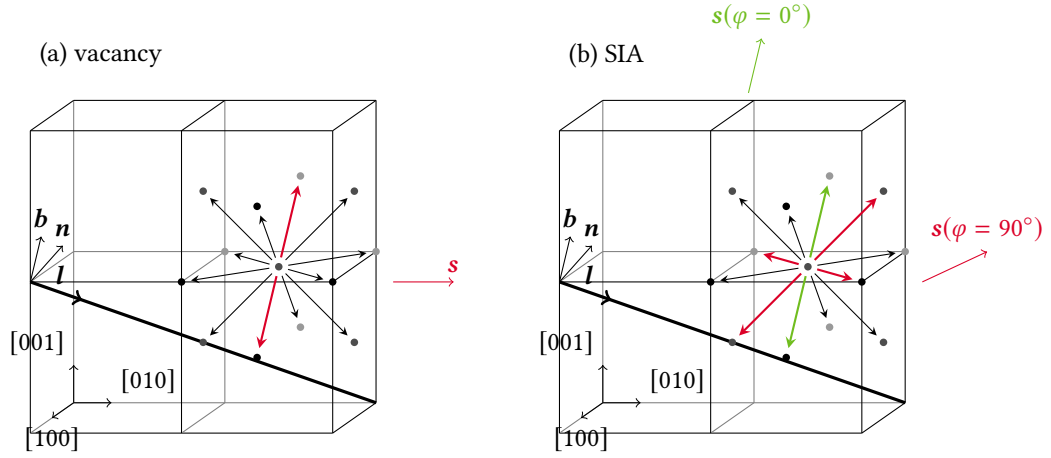


Figure 8: Orientation of uniaxial stress \mathbf{s} leading to maximum absorption of point defects by a dislocation of line direction $\mathbf{l} = [\bar{1}2\bar{1}]/\sqrt{6}$ and Burgers vector $\mathbf{b} = [\bar{1}01]/\sqrt{2}$ ($\mathbf{n} = [111]/\sqrt{3}$), and associated jumps responsible for this high absorption rate. (a) Absorption of vacancies (b) Absorption of SIAs; here we give the orientation of stress if it is applied in the planes defined by (\mathbf{l}, \mathbf{b}) ($\varphi = 0^\circ$) and (\mathbf{l}, \mathbf{n}) ($\varphi = 90^\circ$). The maximum absorption rate is obtained in this latest case, with four jumps contributing significantly to the absorption of SIAs.

533 at saddle configuration are the highest. In the model developed by Borodin
 534 and Ryazanov, the deviatoric part of the dipole tensor is assumed to be small
 535 compared to the hydrostatic part. This is not true for the vacancy, so it is not
 536 surprising that the model cannot quantitatively reproduce the values of ΔZ^{AD}
 537 when the dipole anisotropy contributes significantly to the absorption efficiency.

538 4.3.2. SIPA-I

539 Contrary to SIPA-AD, the dislocation strain field is an essential ingredient
 540 in SIPA-I. The fourth term in Eq. (4), which induces a coupling between the
 541 applied field and the dislocation field, gives rise to preferential diffusion of point
 542 defects to some dislocations. Usually, one considers that SIAs are the main
 543 contributors to SIPA-I, due to their large polarizability [75, 76, 38, 14, 77].
 544 HSW model (Eqs. (7)-(10)) predicts that SIAs will be absorbed preferentially by
 545 dislocations whose Burgers vector is aligned with the applied stress [22, 23, 38].

546 Our DFT calculations confirm that SIAs are much more polarizable than

547 vacancies (Tab. 1). Shear polarizabilities of SIAs and vacancies at stable point,
 548 which are used in the analytical model, are found to differ by around one order
 549 of magnitude. However, the effect of vacancies on SIPA-I is not completely neg-
 550 ligible (Fig. 5): the amplitude of the effect is only three times smaller than for
 551 SIAs. This is essentially due to the high absorption efficiency of vacancies when
 552 the stress is applied in the plane (\mathbf{l}, \mathbf{n}) , for $\theta = 25^\circ$, close to the direction corre-
 553 sponding to a maximum of absorption efficiency for SIPA-AD ($\theta = 33^\circ$). This
 554 behavior is not captured by HSW model. Additional calculations (not shown)
 555 performed with CDM and using isotropic and identical properties at stable and
 556 saddle points led to results in close agreement with HSW model. We can con-
 557 clude that this model is accurate in its framework and that the discrepancy
 558 observed here is certainly due to lattice effects. On the contrary, the agreement
 559 between the model and CDM is rather satisfactory for SIAs, although some
 560 discrepancies appear if the stress is not normal to the dislocation line. This
 561 shows that in general, since polarizabilities induce second order contributions,
 562 they should not be considered without taking into account the first order con-
 563 tributions, *i.e.* of dipole anisotropy. To our knowledge, our simulations are
 564 the first estimations of SIPA-I based on full account of first order terms and
 565 polarizabilities at saddle configurations.

566 As for SIPA-AD, other terms potentially contributing to SIPA are included
 567 in CDM but not in the model. The first part of the seventh term in Eq. (4)
 568 leads to anisotropic diffusion, so to SIPA. However, for applied strains of the
 569 order of 10^{-4} as those considered here, this term can be safely neglected.

570 *4.3.3. Relative contributions of SIPA-AD and SIPA-I to dislocation climb under* 571 *stress*

572 From analytical expressions as (6) and (11), it has been suggested that SIPA-
 573 AD is up to thirty times larger than SIPA-I [14, 12, 16]. It is interesting to see
 574 whether the present calculations, with more accurate values of dipole tensors
 575 and polarizabilities, confirm this conclusion. Indeed, considering polarizabilities
 576 induces additional complexity in kinetic codes, so it is useful to assess the rel-

577 evance of including them. From Figs. 2 and 5, one sees that the amplitude of
578 absorption efficiencies considering intrinsic dipole anisotropy only (SIPA-AD) is
579 around five times larger than the one due to polarizability (SIPA-I), whatever
580 the defect. However, as shown in Fig. 9, for a stress applied in a plane normal
581 to the dislocation line, polarizability reverses the directions of favored absorp-
582 tion of SIAs. The reason for this is the low effect of dipole anisotropy in this
583 plane, at variance with polarizability. This suggests that polarizabilities cannot
584 be disregarded for studies under stress.

585 Including intrinsic dipole anisotropy and polarizability in the calculations
586 permits to conclude about the directions of applied stress which favor SIA or
587 vacancy absorption. From the present results it can be concluded that if the
588 stress is approximately orthogonal to the dislocation line, and in particular along
589 the Burgers vector, the net absorption rate of SIAs should be the highest. On
590 the contrary, a uniaxial stress applied close the $\langle 100 \rangle$ direction with the largest
591 projection on the dislocation line should minimize the net absorption rate of
592 SIAs. Since climb velocity under irradiation is generally driven by an excess of
593 absorbed SIAs due to EID, the climb velocity is expected to increase in the first
594 configuration and to decrease in the second one.

595 **5. Conclusion**

596 In this study we have investigated the effect of an applied uniaxial stress on
597 point defect absorption by straight dislocations in aluminum. Elastic dipoles and
598 diaelastic polarizabilities of vacancies and SIAs have been calculated by DFT at
599 stable and saddle points. These parameters have been used in an OKMC code
600 and a CDM model to evaluate absorption efficiencies under stress. Our results
601 confirm that the amplitude of SIPA-I, due to polarizability, is lower than the
602 one of SIPA-AD, due to dipole anisotropy, by a factor of around five. However,
603 the correct behavior of the absorption efficiency in a plane orthogonal to the
604 dislocation line can only be obtained if polarizability is considered, so neglecting
605 polarizability in studies under stress may not be appropriate.

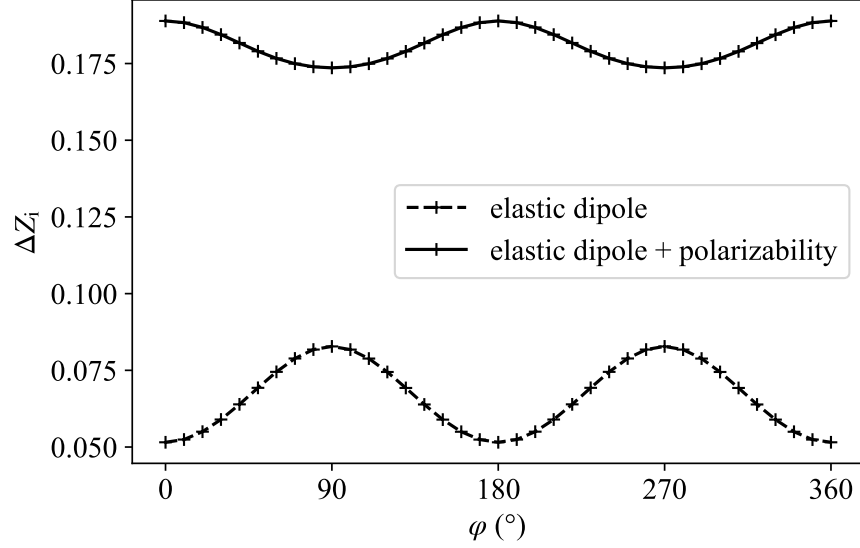


Figure 9: Difference of absorption efficiency of SIA ΔZ_i as a function of φ , calculated with CDM for $\theta = 90^\circ$. The reference calculation which is subtracted corresponds to a hydrostatic stress with only P_{ij} taken into account. The dashed curve shows the evolution of ΔZ_i if only P_{ij} is taken into account and the solid curve corresponds to the case where P_{ij} and α_{ijkl} are considered.

606 Simulation results have been compared to analytical expressions of SIPA-
 607 AD and SIPA-I. For SIA, models are shown to be in reasonable agreement
 608 with simulations. Vacancies are very anisotropic in their saddle configuration,
 609 which induces strong lattice effects on the diffusion under stress. In this case
 610 the predictions of the models are not very accurate. The expression of Borodin
 611 and Ryazanov (B&R) for SIPA-AD includes lattice effects but it is assumed
 612 that defects are weakly anisotropic in their saddle configuration. It correctly
 613 predicts a maximum absorption rate of vacancies if the stress is applied along
 614 the $\langle 100 \rangle$ direction with the largest projection on the dislocation line. However,
 615 the amplitude of SIPA-AD is underestimated by a factor 3. The expression
 616 for SIPA-I given by Woo (HSW model) relies on a simple isotropic description
 617 of defects and is unable to reproduce the angular dependence of absorption

618 efficiency, which is similar to that of SIPA-AD.

619 Our results show that dislocation climb velocity under irradiation is expected
 620 to be the highest if the stress is approximately orthogonal to the dislocation
 621 line, especially along the Burgers vector, and the lowest if the stress is applied
 622 close to the $\langle 100 \rangle$ direction with the largest projection on the dislocation line.
 623 The dependence of these results on the symmetries of point defects in their
 624 saddle configuration makes these conclusions likely transferable to other fcc
 625 metals. The methodology used in this work can be applied to Frank dislocation
 626 loops. It would be interesting to compare the obtained results to experimental
 627 measurements of loop growth rates under stress [7], to better assess irradiation
 628 creep mechanisms.

629 Appendix A. Modelling point defects as inhomogeneous inclusions

630 SIPA-I expressions (6)-(10) are more often given with notations related to
 631 Eshelby inhomogeneous inclusions. In this framework, a defect is considered as
 632 a spherical inhomogeneity of bulk and shear moduli K^* and μ^* , respectively,
 633 with a misfit corresponding to the transformation strain e_{ij}^* . It is convenient to
 634 consider an equivalent homogeneous inclusion of transformation strain e_{ij}^T , which
 635 depends on e_{ij}^* and on the local external strain field (sum of the dislocation and
 636 applied strain fields), as well as on the elastic moduli of the inclusion and of the
 637 matrix [78]. The elastic dipole is related to the equivalent transformation strain
 638 through [29]

$$P_{ij} = \Omega C_{ijkl} e_{kl}^T, \quad (\text{A.1})$$

639 with

$$C_{ijkl} = \left(K - \frac{2}{3}\mu \right) \delta_{ij}\delta_{kl} + \mu (\delta_{ik}\delta_{jl} + \delta_{il}\delta_{jk}). \quad (\text{A.2})$$

640 In SIPA-I models, the defect is considered as isotropic, so $e_{kl}^T = \delta_{kl}e^T/3$. We
 641 obtain

$$P_{ij} = \Omega K e^T \delta_{ij} = P \delta_{ij}, \quad (\text{A.3})$$

642 where P is the quantity used in Eqs. (6)-(10). It is customary to use the strain
 643 within the inclusion in the absence of external field, e_{ij}^0 , related to e_{ij}^T by [78]

$$e_{ij}^0 = \mathcal{S}_{ijkl} e_{kl}^T, \quad (\text{A.4})$$

644 where \mathcal{S}_{ijkl} is the Eshelby tensor for a spherical inclusion:

$$\mathcal{S}_{ijkl} = \frac{5\nu - 1}{15(1 - \nu)} \delta_{ij} \delta_{kl} + \frac{4 - 5\nu}{15(1 - \nu)} (\delta_{ik} \delta_{jl} + \delta_{il} \delta_{jk}). \quad (\text{A.5})$$

645 The strain within the inclusion can be written as $e_{kl}^0 = \delta_{kl} e^0/3$, with

$$e^0 = \frac{1 + \nu}{3(1 - \nu)} e^T = \frac{1 + \nu}{3(1 - \nu)} \frac{P}{\Omega K}. \quad (\text{A.6})$$

646 We note that owing to Eqs. (17) and (A.3), e^T is the normalized relaxation
 647 volume in a finite medium $\Delta V^r/\Omega$, whereas e^0 is the normalized relaxation
 648 volume in an infinite medium $\Delta V^\infty/\Omega$, the deformation being localized at the
 649 position of the point defect [79].

650 By comparing the expressions of the interaction energy given by Eshelby [78]
 651 and the one obtained from Eqs. (2) and (5), the following expressions are ob-
 652 tained:

$$\alpha^K = -K\Omega \frac{3(1 - \nu)\Delta K}{3(1 - \nu)K + (1 + \nu)\Delta K} \quad (\text{A.7})$$

$$\alpha^\mu = -\mu\Omega \frac{15(1 - \nu)\Delta\mu}{15(1 - \nu)\mu + 2(4 - 5\nu)\Delta\mu}, \quad (\text{A.8})$$

653 with $\Delta K = K^* - K$ and $\Delta\mu = \mu^* - \mu$.

654 **Appendix B. Set of deformation types to calculate polarizability ten-** 655 **sors**

656 The structure of the polarizability tensors of vacancies and SIAs in their
 657 stable and saddle configurations depend on their symmetries. They are given in
 658 Table B.2. To determine all coefficients, we consider several deformation types
 659 (Tab. B.3). Since both initial ([100]) and final ([010]) configurations must be
 660 relaxed under applied strain in order to calculate the saddle position, the results

Table B.2: Structure of polarizability tensors of vacancies and SIAs in their stable and saddle configurations.

	Stable configuration	Saddle configuration
	Cubic symmetry	Orthorhombic symmetry
Vacancy		For [100] to [010] jump
	$\begin{pmatrix} \alpha_{11} & \alpha_{12} & \alpha_{12} & 0 & 0 & 0 \\ \alpha_{12} & \alpha_{11} & \alpha_{12} & 0 & 0 & 0 \\ \alpha_{12} & \alpha_{12} & \alpha_{11} & 0 & 0 & 0 \\ 0 & 0 & 0 & \alpha_{44} & 0 & 0 \\ 0 & 0 & 0 & 0 & \alpha_{44} & 0 \\ 0 & 0 & 0 & 0 & 0 & \alpha_{44} \end{pmatrix}$	$\begin{pmatrix} \alpha_{11} & \alpha_{12} & \alpha_{13} & 0 & 0 & \alpha_{16} \\ \alpha_{12} & \alpha_{11} & \alpha_{13} & 0 & 0 & \alpha_{16} \\ \alpha_{13} & \alpha_{13} & \alpha_{33} & 0 & 0 & \alpha_{36} \\ 0 & 0 & 0 & \alpha_{44} & \alpha_{45} & 0 \\ 0 & 0 & 0 & \alpha_{45} & \alpha_{44} & 0 \\ \alpha_{16} & \alpha_{16} & \alpha_{36} & 0 & 0 & \alpha_{66} \end{pmatrix}$
	Tetragonal symmetry	Orthorhombic symmetry
SIA	For [100] configuration	For [100] to [010] jump
	$\begin{pmatrix} \alpha_{11} & \alpha_{12} & \alpha_{12} & 0 & 0 & 0 \\ \alpha_{12} & \alpha_{22} & \alpha_{23} & 0 & 0 & 0 \\ \alpha_{12} & \alpha_{23} & \alpha_{22} & 0 & 0 & 0 \\ 0 & 0 & 0 & \alpha_{44} & 0 & 0 \\ 0 & 0 & 0 & 0 & \alpha_{55} & 0 \\ 0 & 0 & 0 & 0 & 0 & \alpha_{55} \end{pmatrix}$	$\begin{pmatrix} \alpha_{11} & \alpha_{12} & \alpha_{13} & 0 & 0 & \alpha_{16} \\ \alpha_{12} & \alpha_{11} & \alpha_{13} & 0 & 0 & \alpha_{16} \\ \alpha_{13} & \alpha_{13} & \alpha_{33} & 0 & 0 & \alpha_{36} \\ 0 & 0 & 0 & \alpha_{44} & \alpha_{45} & 0 \\ 0 & 0 & 0 & \alpha_{45} & \alpha_{44} & 0 \\ \alpha_{16} & \alpha_{16} & \alpha_{36} & 0 & 0 & \alpha_{66} \end{pmatrix}$

Table B.3: Strain tensors and related variation in energies and dipole tensors due to polarizability. Tetragonal and orthorhombic symmetries refer to polarizability tensors given in Table B.2 ([100] orientation for the SIA and [100] to [010] jump respectively), unless specified.

strain matrix	cubic symmetry		tetragonal symmetry		orthorhombic symmetry	
	$-\frac{1}{2}\alpha_{ijkl}\varepsilon_j\varepsilon_k\varepsilon_l$	$-V\Delta\sigma_{ij} = \alpha_{ijkl}\varepsilon_k\varepsilon_l$	$-\frac{1}{2}\alpha_{ijkl}\varepsilon_j\varepsilon_k\varepsilon_l$	$-V\Delta\sigma_{ij} = \alpha_{ijkl}\varepsilon_k\varepsilon_l$	$-\frac{1}{2}\alpha_{ijkl}\varepsilon_j\varepsilon_k\varepsilon_l$	$-V\Delta\sigma_{ij} = \alpha_{ijkl}\varepsilon_k\varepsilon_l$
$\varepsilon_1 = \begin{pmatrix} \varepsilon & 0 & 0 \\ 0 & \varepsilon & 0 \\ 0 & 0 & \varepsilon \end{pmatrix}$	$-\frac{3}{2}(\alpha_{11} + 2\alpha_{12})\varepsilon^2$	$-V\Delta\sigma_{11} = (\alpha_{11} + 2\alpha_{12})\varepsilon$	$-\frac{1}{2}(\alpha_{11} + 2\alpha_{22} + 4\alpha_{12} + 2\alpha_{23})\varepsilon^2$	$-V\Delta\sigma_{11} = (\alpha_{11} + 2\alpha_{12})\varepsilon$ $-V\Delta\sigma_{22} = (\alpha_{12} + \alpha_{22} + \alpha_{23})\varepsilon$	$-\frac{1}{2}(2\alpha_{11} + 2\alpha_{12} + \alpha_{33} + 4\alpha_{13})\varepsilon^2$	$-V\Delta\sigma_{11} = (\alpha_{11} + \alpha_{12} + \alpha_{13})\varepsilon$ $-V\Delta\sigma_{33} = (2\alpha_{13} + \alpha_{33})\varepsilon$ $-V\Delta\sigma_{12} = (2\alpha_{16} + \alpha_{36})\varepsilon$
$\varepsilon_2 = \begin{pmatrix} \varepsilon & 0 & 0 \\ 0 & 0 & 0 \\ 0 & 0 & 0 \end{pmatrix}$	$-\frac{1}{2}\alpha_{11}\varepsilon^2$	$-V\Delta\sigma_{11} = \alpha_{11}\varepsilon$ $-V\Delta\sigma_{22} = \alpha_{12}\varepsilon$	$\frac{1}{2}\alpha_{11}\varepsilon^2$ $\frac{1}{2}\alpha_{22}\varepsilon^2$ $-\frac{1}{2}\alpha_{23}\varepsilon^2$ ^(a)	$-V\Delta\sigma_{11} = \alpha_{11}\varepsilon$ $-V\Delta\sigma_{22} = \alpha_{12}\varepsilon$ $-V\Delta\sigma_{11} = \alpha_{22}\varepsilon$ ^(a) $-V\Delta\sigma_{22} = \alpha_{12}\varepsilon$ ^(a) $-V\Delta\sigma_{33} = \alpha_{23}\varepsilon$ ^(a)	$-\frac{1}{2}\alpha_{11}\varepsilon^2$	$-V\Delta\sigma_{11} = \alpha_{11}\varepsilon$ $-V\Delta\sigma_{22} = \alpha_{12}\varepsilon$ $-V\Delta\sigma_{33} = \alpha_{13}\varepsilon$ $-V\Delta\sigma_{12} = \alpha_{16}\varepsilon$
$\varepsilon_3 = \begin{pmatrix} 0 & 0 & 0 \\ 0 & 0 & \varepsilon \\ 0 & \varepsilon & 0 \end{pmatrix}$	$-2\alpha_{44}\varepsilon^2$	$-V\Delta\sigma_{23} = 2\alpha_{44}\varepsilon$	$-2\alpha_{44}\varepsilon^2$ $-2\alpha_{35}\varepsilon^2$ ^(a)	$-V\Delta\sigma_{23} = 2\alpha_{44}\varepsilon$ $-V\Delta\sigma_{23} = 2\alpha_{55}\varepsilon$ ^(a)	$-2\alpha_{44}\varepsilon^2$	$-V\Delta\sigma_{23} = 2\alpha_{44}\varepsilon$ $-V\Delta\sigma_{13} = 2\alpha_{45}\varepsilon$
$\varepsilon_4 = \begin{pmatrix} 0 & \varepsilon & 0 \\ \varepsilon & 0 & 0 \\ 0 & 0 & 0 \end{pmatrix}$		Equivalent to ε_3	Equivalent to ε_3 on final configuration		$-2\alpha_{66}\varepsilon^2$	$-V\Delta\sigma_{11} = 2\alpha_{16}\varepsilon$ $-V\Delta\sigma_{33} = 2\alpha_{36}\varepsilon$ $-V\Delta\sigma_{12} = 2\alpha_{66}\varepsilon$

^(a) On final configuration (SIA oriented along [010])

661 concerning the final configurations can also be exploited to obtain additional
 662 data about coefficients of the polarizability tensor.

663 Figures B.10 and B.11 show the variation of energy due to polarizability,
 664 called $E^{(2)}$ (see Tab. B.3) extracted from DFT simulations (solid lines) and
 665 calculated with the elastic model using polarizabilities deduced from residual
 666 stress (in dashed lines). The variation of residual stress due to polarizabil-
 667 ity, $-V\Delta\sigma_{ij} = \alpha_{ijkl}\varepsilon_{kl}$, is also shown. These two deformations (1 and 3, see
 668 Tab. B.3) correspond to dilatation/compression and $\langle 100 \rangle$ shear.

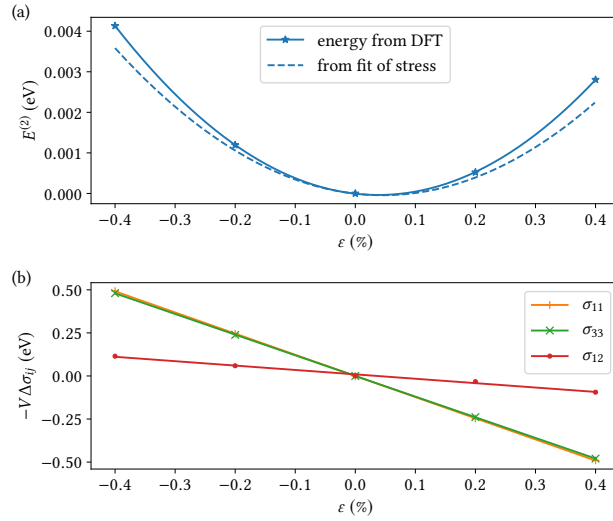


Figure B.10: Deformation 1 (dilatation/compression): (a) Variation of energy due to polarizability, extracted from DFT simulations (symbols with fit in solid lines) and calculated with the elastic model using polarizabilities extracted from residual stress (dashed lines). (b) Variation of residual stress (*i. e.* change in dipole tensors) due to polarizability, which is fitted with a linear function to extract polarizabilities.

669 Acknowledgments

670 T. J. acknowledges F. Willaime for discussions about DFT calculations and
 671 Y. Le Bouar for discussions about polarizabilities. This work was performed
 672 using HPC resources from GENCI-CINES (Grant 2020-A0100912414).

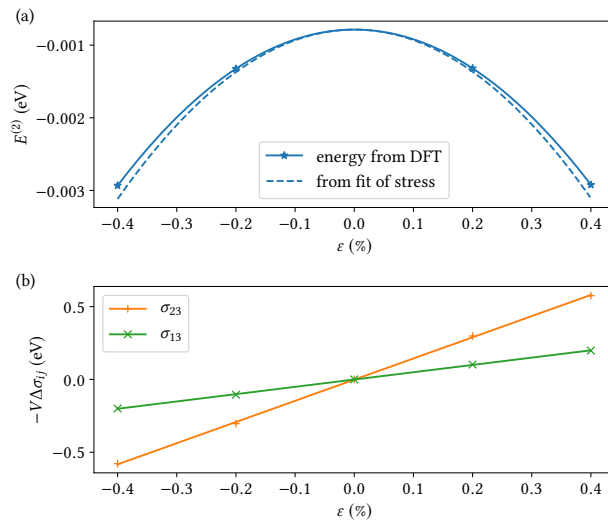


Figure B.11: Deformation 3 ((100) shear): (a) Variation of energy due to polarizability, extracted from DFT simulations (symbols with fit in solid lines) and calculated with the elastic model using polarizabilities extracted from residual stress (dashed lines). (b) Variation of residual stress (*i. e.* change in dipole tensors) due to polarizability, which is fitted with a linear function to extract polarizabilities.

673 **Data availability**

674 The relevant data are available within the article or from the authors upon
675 reasonable request.

676 **References**

- 677 [1] J. R. Matthews, M. W. Finnis, Irradiation creep models – An overview, J.
678 Nucl. Mater. 159 (1988) 257.
- 679 [2] F. Onimus, T. Jourdan, C. Xu, A. A. Campbell, M. Griffiths, 1.10 - irra-
680 diation creep in materials, in: Comprehensive Nuclear Materials, Elsevier,
681 2020, p. 310.
- 682 [3] P. R. Okamoto, S. D. Harkness, Stress-biased loop nucleation in irradiated
683 type 316 stainless steels, J. Nucl. Mater. 48 (1973) 204.
- 684 [4] F. A. Garner, W. G. Wolfer, H. R. Brager, A reassessment of the role
685 of stress in development of radiation-induced microstructure, in: J. A.
686 Sprague, D. Kramer (Eds.), Effects of radiation on structural materials,
687 ASTM STP 683, 1979, p. 160.
- 688 [5] D. Faulkner, R. J. McElroy, Irradiation creep and growth in zirconium
689 during proton bombardment, in: J. A. Sprague, D. Kramer (Eds.), Effects
690 of Radiation on Structural Materials: ASTM STP 683, 1979, p. 329.
- 691 [6] F. A. Garner, D. S. Gelles, Irradiation creep mechanisms: an experimental
692 perspective, J. Nucl. Mater. 159 (1988) 286.
- 693 [7] S. Jitsukawa, Y. Katano, K. Shiraishi, F. A. Garner, The Behavior of
694 Irradiation-Produced Dislocation Loops under External Stress during Elec-
695 tron Irradiation, in: R. E. Stoller, A. S. Kumar, D. S. Gelles (Eds.), Effects
696 of Radiation on Materials: 15th International Symposium, 1992, p. 1034.
- 697 [8] C. Xu, G. S. Was, Anisotropic dislocation loop distribution in alloy T91
698 during irradiation creep, J. Nucl. Mater. 454 (2014) 255.

- 699 [9] W. G. Wolfer, Correlation of radiation creep theory with experimental ev-
700 idence, *J. Nucl. Mater.* 90 (1980) 175.
- 701 [10] W. G. Wolfer, L. K. Mansur, J. A. Sprague, Theory of swelling and irradi-
702 ation creep, in: M. L. Bleiberg, J. W. Bennett (Eds.), *Radiation Effects in*
703 *Breeder Reactor Structural Materials*, 1977, p. 479.
- 704 [11] L. K. Mansur, Irradiation creep by climb-enabled glide of dislocations re-
705 sulting from preferred absorption of point defects, *Philos. Mag. A* 39 (1979)
706 497.
- 707 [12] C. H. Woo, E. J. Savino, Stress-induced preferred absorption due to saddle-
708 point anisotropy: the case of an infinitesimal dislocation loop, *J. Nucl.*
709 *Mater.* 116 (1983) 17.
- 710 [13] B. C. Skinner, C. H. Woo, Shape effect in the drift diffusion of point defects
711 into straight dislocations, *Phys. Rev. B* 30 (1984) 3084.
- 712 [14] E. J. Savino, C. N. Tomé, Irradiation creep by stress-induced preferential
713 attraction due to anisotropic diffusion (SIPA-AD), *J. Nucl. Mater.* 108 &
714 109 (1982) 405.
- 715 [15] C. N. Tomé, H. A. Cecatto, E. J. Savino, Point-defect diffusion in a strained
716 crystal, *Phys. Rev. B* 25 (1982) 7428.
- 717 [16] C. H. Woo, Irradiation creep due to elastodiffusion, *J. Nucl. Mater.* 120
718 (1984) 55.
- 719 [17] V. A. Borodin, A. I. Ryazanov, The effect of diffusion anisotropy on dislo-
720 cation bias and irradiation creep in cubic lattice materials, *J. Nucl. Mater.*
721 210 (1994) 258.
- 722 [18] H. R. Schober, Single and multiple interstitials in FCC metals, *J. Phys. F:*
723 *Metal Phys.* 7 (1977) 1127.
- 724 [19] E. J. Savino, Point defect-dislocation interaction in a crystal under tension,
725 *Philos. Mag.* 36 (1977) 323.

- 726 [20] P. H. Dederichs, K. Schroeder, Anisotropic diffusion in stress fields, *Phys.*
727 *Rev. B* 17 (1978) 2524.
- 728 [21] P. T. Heald, M. V. Speight, Steady-state irradiation creep, *Philos. Mag.* 29
729 (1974) 1075.
- 730 [22] R. Bullough, J. R. Willis, The stress-induced point defect-dislocation in-
731 teraction and its relevance to irradiation creep, *Philos. Mag.* 31 (1975) 855.
- 732 [23] P. T. Heald, M. V. Speight, Point defect behaviour in irradiated materials,
733 *Acta Metall.* 23 (1975) 1389.
- 734 [24] W. Schilling, Self-interstitial atoms in metals, *J. Nucl. Mater.* 69 & 70
735 (1978) 465.
- 736 [25] C. Varvenne, E. Clouet, Elastic dipoles of point defects from atomistic
737 simulations, *Phys. Rev. B* 96 (2017) 224103.
- 738 [26] D. Carpentier, T. Jourdan, Y. Le Bouar, M.-C. Marinica, Effect of saddle
739 point anisotropy of point defects on their absorption by dislocations and
740 cavities, *Acta Mater.* 136 (2017) 323.
- 741 [27] T. Jourdan, A. Vattré, A continuous model including elastodiffusion for
742 sink strength calculation of interfaces, *Comput. Mater. Sci.* 153 (2018) 473.
- 743 [28] R. Siems, Mechanical interactions of point defects, *Phys. Stat. Sol.* 30
744 (1968) 645.
- 745 [29] E. Clouet, C. Varvenne, T. Jourdan, Elastic modeling of point-defects and
746 their interactions, *Comp. Mater. Sci.* 147 (2018) 49.
- 747 [30] H. R. Schober, Polarizabilities of point defects in metals, *J. Nucl. Mater.*
748 126 (1984) 220.
- 749 [31] A. D. Brailsford, R. Bullough, The rate theory of swelling due to void
750 growth in irradiated metals, *J. Nucl. Mater.* 44 (1972) 121.

- 751 [32] A. D. Brailsford, R. Bullough, M. R. Hayns, Point defect sink strengths
752 and void-swelling, *J. Nucl. Mater.* 60 (1976) 246–256.
- 753 [33] F. A. Nichols, On the estimation of sink-absorption terms in reaction-rate-
754 theory analysis of radiation damage, *J. Nucl. Mater.* 75 (1978) 32.
- 755 [34] C. H. Woo, The sink strength of a dislocation loop in the effective medium
756 approximation, *J. Nucl. Mater.* 98 (1981) 279.
- 757 [35] T. Jourdan, Influence of dislocation and dislocation loop biases on mi-
758 crostructures simulated by rate equation cluster dynamics, *J. Nucl. Mater.*
759 467 (2015) 286.
- 760 [36] A. A. Kohnert, L. Capolungo, Sink strength and dislocation bias of three-
761 dimensional microstructures, *Phys. Rev. Mater.* 3 (2019) 053608.
- 762 [37] W. G. Wolfer, M. Ashkin, Diffusion of vacancies and interstitials to edge
763 dislocations, *J. Appl. Phys.* 47 (1976) 791.
- 764 [38] C. H. Woo, Effects of an anisotropic dislocation structure on irradiation
765 creep due to stress induced preferred absorption of point defects, *J. Nucl.*
766 *Mater.* 80 (1979) 132.
- 767 [39] P. Ehrhart, P. Jung, H. Schultz, H. Ullmaier, Landolt–Börnstein, Numeri-
768 cal Data and Functional Relationships in Science and Technology, Atomic
769 Defects In Metals, Springer, 1991.
- 770 [40] I.-W. Chen, Anisotropic diffusion of point defects to edge dislocations, *J.*
771 *Nucl. Mater.* 125 (1984) 52.
- 772 [41] G. F. Bouobda Moladje, L. Thuinet, C. Domain, C. S. Becquart, A. Legris,
773 Phase-field calculations of sink strength in Al, Ni, and Fe: A detailed study
774 of elastic effects, *Comput. Mater. Sci.* 183 (2020) 109905.
- 775 [42] V. A. Borodin, The effect of swelling on SIPA irradiation creep, *J. Nucl.*
776 *Mater.* 225 (1995) 15.

- 777 [43] A. Vattré, T. Jourdan, H. Ding, M.-C. Marinica, M. J. Demkowicz, Non-
778 random walk diffusion enhances the sink strength of semicoherent inter-
779 faces, *Nat. Commun.* 7 (2016) 10424.
- 780 [44] E. Clouet, A. Bakaev, V. Borodin, Z. Chang, C. C. Fu, M. C. Marinica,
781 P. Olsson, M. Posselt, D. Terentyev, P. Vladimirov, E. E. Zhurkin, Screen-
782 ing of irradiation creep mechanisms using atomic-level simulation tools,
783 Tech. rep., MATISSE project (2017).
784 URL <http://fp7-matisse.eu/public-project-reports/>
- 785 [45] E. Clouet, S. Garruchet, H. Nguyen, M. Perez, C. S. Becquart, Dislocation
786 interaction with C in α -Fe: A comparison between atomic simulations and
787 elastic theory, *Acta Mater.* 56 (2008) 3450.
- 788 [46] G. Kresse, J. Hafner, *Ab initio* molecular dynamics for liquid metals, *Phys.*
789 *Rev. B* 47 (1993) 558.
- 790 [47] G. Kresse, J. Hafner, *Ab initio* molecular-dynamics simulation of the liquid-
791 metal–amorphous-semiconductor transition in germanium, *Phys. Rev. B* 49
792 (1994) 14251.
- 793 [48] G. Kresse, J. Furthmüller, Efficiency of ab-initio total energy calcula-
794 tions for metals and semiconductors using a plane-wave basis set, *Comput.*
795 *Mater. Sci.* 6 (1996) 15.
- 796 [49] G. Kresse, J. Furthmüller, Efficient iterative schemes for *ab initio* total-
797 energy calculations using a plane-wave basis set, *Phys. Rev. B* 54 (1996)
798 11169.
- 799 [50] P. E. Blöchl, Projector augmented-wave method, *Phys. Rev. B* 50 (1994)
800 17953.
- 801 [51] G. Kresse, D. Joubert, From ultrasoft pseudopotentials to the projector
802 augmented-wave method, *Phys. Rev. B* 59 (1999) 1758.

- 803 [52] N. Chetty, M. Weinert, T. S. Rahman, J. W. Davenport, Vacancies and
804 impurities in aluminum and magnesium, *Phys. Rev. B* 52 (9) (1995) 6313.
- 805 [53] G. Henkelman, B. P. Uberuaga, H. Jónsson, A climbing image nudged
806 elastic band method for finding saddle points and minimum energy paths,
807 *J. Chem. Phys.* 113 (2000) 9901.
- 808 [54] M. A. Caro, S. Schulz, E. P. O'Reilly, Comparison of stress and total energy
809 methods for calculation of elastic properties of semiconductors, *J. Phys.:*
810 *Condens. Matter* 25 (2013) 025803.
- 811 [55] D. Connétable, P. Maugis, Effect of stress on vacancy formation and diffu-
812 sion in fcc systems: Comparison between DFT calculations and elasticity
813 theory, *Acta Mater.* 200 (2020) 869.
- 814 [56] V. Spirić, L. E. Rehn, K.-H. Robrock, W. Schilling, Anelastic relaxation
815 due to single self-interstitial atoms in electron-irradiated Al, *Phys. Rev. B*
816 15 (1977) 672.
- 817 [57] K.-H. Robrock, W. Schilling, Diaelastic modulus change of aluminum after
818 low temperature electron irradiation, *J. Phys. F: Metal Phys.* 6 (3) (1976)
819 303.
- 820 [58] P. H. Dederichs, C. Lehmann, A. Scholz, Change of elastic constants due
821 to interstitials, *Z. Physik B* 20 (1975) 155.
- 822 [59] J. Holder, A. V. Granato, L. E. Rehn, Effects of self-interstitials and close
823 pairs on the elastic constants of copper, *Phys. Rev. B* 10 (2) (1974) 363.
- 824 [60] L. E. Rehn, J. Holder, A. V. Granato, R. R. Coltman, F. W. Young, Jr,
825 Effects of thermal-neutron irradiation on the elastic constants of copper,
826 *Phys. Rev. B* 10 (2) (1974) 349.
- 827 [61] M. P. Puls, C. H. Woo, Diaelastic polarizabilities due to vacancies and
828 interstitials in metals, *J. Nucl. Mater.* 139 (1986) 48.

- 829 [62] G. J. Ackland, Theoretical study of the effect of point defects on the elastic
830 constants of copper, *J. Nucl. Mater.* 152 (1988) 53.
- 831 [63] H.-G. Haubold, Study of irradiation induced point defects by diffuse scat-
832 tering, in: *Proc. Int. Conf. Fundamental Aspects of Radiation Damage in*
833 *Metals*, 1975, p. 268.
- 834 [64] R. M. Emrick, P. B. McArdle, Effect of pressure on quenched-in electrical
835 resistance in gold and aluminum, *Phys. Rev.* 188 (1969) 1156.
- 836 [65] P. Ehrhart, W. Schilling, Investigation of interstitials in electron-irradiated
837 aluminum by diffuse-X-ray scattering experiments, *Phys. Rev. B* 8 (6)
838 (1973) 2604.
- 839 [66] B. J. Buescher, R. M. Emrick, Pressure effect on defect migration in alu-
840 minum, *Phys. Rev. B* 1 (10) (1970) 3922.
- 841 [67] R. C. Folweiler, F. R. Brotzen, The effect of quenched-in vacancies on the
842 elastic modulus of aluminum, *Acta Metall.* 7 (1959) 716.
- 843 [68] H. R. Brager, F. A. Garner, E. R. Gilbert, J. E. Flinn, W. G. Wolfer,
844 Stress-affected microstructural development and the creep-swelling interre-
845 lationship, in: M. L. Bleiberg, J. W. Bennett (Eds.), *Radiation Effects in*
846 *Breeder Reactor Structural Materials*, The Metallurgical Society of AIME,
847 1977, p. 727.
- 848 [69] W. P. Kuykendall, W. Cai, Conditional convergence in two-dimensional
849 dislocation dynamics, *Modelling Simul. Mater. Sci. Eng.* 21 (2013) 055003.
- 850 [70] D. T. Gillespie, A general method for numerically simulating the stochastic
851 time evolution of coupled chemical reactions, *J. Comput. Phys.* 22 (1976)
852 403.
- 853 [71] A. B. Bortz, M. H. Kalos, J. L. Lebowitz, A New Algorithm for Monte-
854 Carlo Simulation of Ising Spin Systems, *J. Comput. Phys.* 17 (1975) 10.

- 855 [72] B. Zhang, C. Wheatley, P. Chen, X. Qian, M. J. Demkowicz, Shear strain
856 alters the structure and migration of self-interstitial atoms in copper, *Phys.*
857 *Rev. Mater.* 6 (2022) 053605.
- 858 [73] H. Flyvbjerg, H. G. Petersen, Error estimates on averages of correlated
859 data, *J. Chem. Phys.* 91 (1989) 461.
- 860 [74] C. H. Woo, Intrinsic bias differential between vacancy loops and interstitial
861 loops, *J. Nucl. Mater.* 107 (1982) 20.
- 862 [75] R. Bullough, M. R. Hayns, Irradiation-creep due to point defect absorption,
863 *J. Nucl. Mater.* 57 (1975) 348.
- 864 [76] P. T. Heald, Radiation-induced creep and swelling, in: M. L. Bleiberg, J. W.
865 Bennett (Eds.), *Radiation Effects in Breeder Reactor Structural Materials*,
866 1977, p. 781.
- 867 [77] C. Xu, G. S. Was, Proton irradiation creep of FM steel T91, *J. Nucl. Mater.*
868 459 (2015) 183.
- 869 [78] J. D. Eshelby, The determination of the elastic field of an ellipsoidal inclu-
870 sion, and related problems, *Proceedings of the Royal Society of London.*
871 *Series A. Mathematical and Physical Sciences* 241 (1957) 376.
- 872 [79] G. Leibfried, N. Breuer, *Point Defects in Metals I*, in: *Springer Tracts in*
873 *Modern Physics*, Springer-Verlag, Berlin, 1978.